Ore Geology Reviews 58 (2014) 27–40

Contents lists available at ScienceDirect

Ore Geology Reviews

journal homepage: www.elsevier.com/locate/oregeorev

The fault-controlled skarn W–Mo polymetallic mineralization during the main India–Eurasia collision: Example from Hahaigang deposit of Gangdese metallogenic belt of Tibet

Xiaofeng Li [a,*], Chunzeng Wang [b], Wei Mao [a], Qinghong Xu [c], Yaohui Liu [c]

[a] State Key Laboratory of Ore Deposit Geochemistry, Institute of Geochemistry, Chinese Academy of Sciences, Guiyang, Guizhou 550002, China
[b] University of Maine at Presque Isle, Presque Isle, ME 04769, USA
[c] Guilin Research Institute of Geology for Mineral Resources, Guilin, Guangxi 541004, China

ARTICLE INFO

Article history:
Received 9 June 2013
Received in revised form 26 October 2013
Accepted 28 October 2013
Available online 6 November 2013

Keywords:
W–Mo polymetallic mineralization
Skarn
Ilvaite
Geochronology
India–Eurasia collision
Hahaigang deposit
Gangdese Belt
Tibet

ABSTRACT

The Hahaigang W–Mo polymetallic skarn deposit is located in the central-eastern part of Gangdese tectono-magmatic belt in Lhasa terrane, Tibet. The deposit was discovered in 2007 with currently proven 46 million tons of WO_3 ores, 12 million tons of Mo ores, and 1.31 million tons of combined Cu–Pb–Zn ores, at an average grade of 0.20% WO_3, 0.07% Mo, 0.026% Cu, 0.49% Pb, and 3.1% Zn. Ore bodies occur in veins or disseminations, and are confined within the NE-striking Dalong fault zone which is hosted by the Lower-Permian Pangna Group of dominantly quartz sandstone and slate. Several granitic plutons are exposed in the area or known from drill-holes. Ages of these granitic plutons are determined by using zircon U–Pb LA–ICP–MS method. For example, the biotite monzogranite yields a $^{206}Pb/^{238}U$–$^{207}Pb/^{238}U$ concordia age of 58.66 ± 0.90 Ma and a weighted mean $^{206}Pb/^{238}U$ age of 57.02 ± 0.42 Ma. The granite porphyry yields a $^{206}Pb/^{238}U$–$^{207}Pb/^{238}U$ concordia age of 109.1 ± 8.9 Ma and a weighted mean $^{206}Pb/^{238}U$ age of 114.0 ± 2.6 Ma. The biotite monzogranite yields a weighted mean $^{206}Pb/^{238}U$ age of 56.1 ± 1.1 Ma. Re–Os isochron age of 63.2 ± 3.2 Ma from 5 molybdenite samples collected from the W–Mo skarn ores is also obtained in this study. The zircon U–Pb and molybdenite Re–Os geochronological data suggest that the W–Mo mineralization was not temporally associated with any of the dated igneous plutons. However, the molybdenite Re–Os age of 63.2 ± 3.2 Ma indicates that the W–Mo mineralization might have occurred during the main India–Eurasia collision that was initiated around 65 Ma. Microprobe analysis of ilvaite that occurs in two generations in the W–Mo skarn ores reveals a close relationship to Ca–Fe–F-rich hydrothermal fluids, which were probably derived from deeply-seated magmas. We suggest that ascent of the fluids was strictly controlled by the ore-controlling Dalong fault zone, and that chemical interaction and metasomatism between the fluids and the Lower-Permian Pangna quartz-feldspathic host rocks produced the ilvaite and the W–Mo polymetallic skarn deposit during the main India–Eurasia collision. Although the majority of the polymetallic deposits in the Gangdese belt are reported to be either pre- or post-main collision, it is evident from this study that the main collision also produced W–Mo polymetallic mineralization within the belt.

1. Introduction

The Middle Miocene Gangdese tectono-magmatic belt in the Tibetan plateau is also a significant metallogenic belt in Tibet. Existence and characteristics of the deposits in the Gangdese tectono-magmatic–metallogenic belt provide not only clues for understanding the relationship between tectono-magmatic evolution and mineralization, but also constraints on the temporal–spatial evolution of magmatic and mineralization processes in the Gangdese belt. These deposits include post-collision porphyry Cu and Mo deposits and porphyry-related Cu, Pb, and Zn deposits along the southern part of the Gangdese belt, e.g., Jiama, Dongga, Xiongcun, and Qulong Cu and Au deposits, and the smaller Tingguan, Chongjiang, Dabu, and Lakange deposits. The northern part of the belt is characterized by post-collision porphyry–skarn–hydrothermal W and Mo deposits as well as skarn Ag, Pb, and Zn deposits, including Lawu, Bagala, Mengyaa, and Dongzhongsun deposits (Fig. 1). Generally, Cu-related deposits dominate the southern part of the central-eastern Gangdese tectono-magmatic belt, whereas W-related deposits the northern part (Yan et al., 2010).

The Hahaigang W–Mo polymetallic skarn deposit is located in central-eastern part of the Gangdese tectono-magmatic belt, within the Lhasa terrane, Tibet (Fig. 1). The deposit was discovered in 2007 with proven 46 million tons of WO_3 ores, 12 million tons of Mo ores, and 1.31 million tons of Cu–Pb–Zn polymetallic ores, at an average grade of 0.20% WO_3, 0.07% Mo, 0.026% Cu, 0.49% Pb, and 3.1% Zn (Guilin Research Institute of Geology for Mineral Resources, 2009).

* Corresponding author at: Institute of Geochemistry, Chinese Academy of Sciences, 46 Guanshui Road, Guiyang, Guizhou 550002, China. Tel.: +86 0851 5891199.
E-mail address: x-f-li@hotmail.com (X. Li).

0169-1368/$ – see front matter © 2013 Elsevier B.V. All rights reserved.
http://dx.doi.org/10.1016/j.oregeorev.2013.10.006

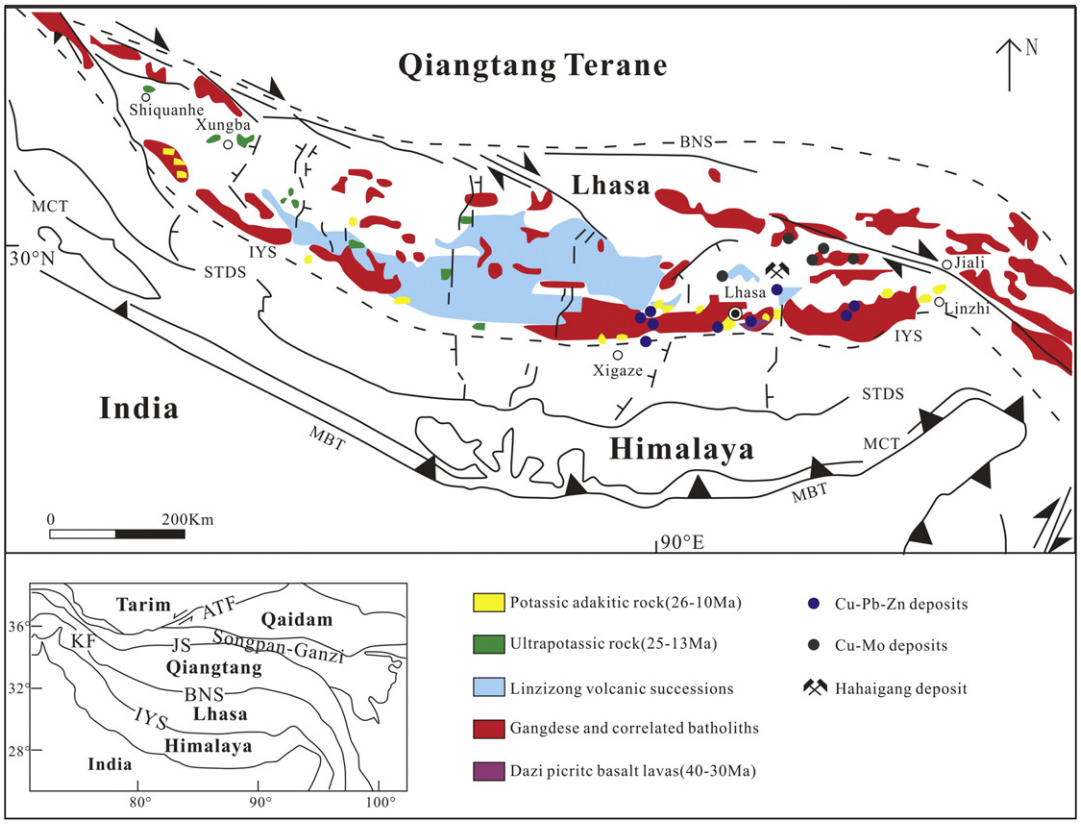

Fig. 1. Map showing simplified tectonic and regional geologic setting of Gangdese tectono-magmatic–metallogenic belt of Tibet (modified after Hou et al., 2013). STDS — South Tibetan Detachment System; ATF — Altyn Tagh Fault; KF — Kunlun Fault. See the text for other abbreviations.

The Hahaigang deposit is currently under development for mining. The deposit is a new member of the recently discovered W–Mo polymetallic deposits in Gangdese tectono-magmatic belt (Hou et al., 2006a, 2006b). Reports of several polymetallic deposits in the Gangdese metallogenic belt have recently been published (Gao et al., 2011; Hou et al., 2009; Yan and Huang, 2010; Yan et al., 2010), for example, the syn-collision porphyry-related Yaguila Pb–Zn–Mo deposit (65.0 ± 1.9 Ma; Gao et al., 2011). However, the age of mineralization, hydrothermal alteration, and genesis of the Hahaigang deposit remain unclear.

In this paper, we report geochronological work on both W–Mo mineralization and related granitic intrusions of the Hahaigang deposit. Molybdenite samples were collected from skarn bodies for Re–Os dating, and zircon samples from granitic intrusions exposed and encountered by drilling in the ore district were for U–Pb dating using LA–ICP–MS method. The goal was to develop an understanding of the temporal relationship between the deposits and the granitic plutons, and to determine the timing of the W–Mo mineralization in the context of the India–Eurasia collision. In this study, a microprobe geochemical analysis of ilvaite that occurs in W-bearing skarn ores of the deposit was also performed in order to understand the contribution of Ca- and Fe-rich fluids to W and Mo mineralization process.

2. Regional tectonic and geologic setting

The Hahaigang W–Mo polymetallic deposit is geographically situated 50 km north of Maizhokunggar County in central Tibet, and tectonically located within the Gangdese tectono-magmatic belt in the Lhasa terrane. The Gangdese belt, about 2000 km long and 100–300 km wide, is sandwiched by two east–west-striking suture zones, i.e., the Bangong–Nujiang suture zone (BNS) in the north and the Indus–Yarlung suture zone (IYS) in the south. The Gangdese belt is a major component of the Himalayan–Tibetan orogen which resulted from complex tectonic collage of several accreted terranes, including the Songpan–Ganzê, Qiangtang, and Lhasa terranes that are bounded from north to south by Jinsha (JS), Bangong–Nujiang (BNS), and Indus–Yarlung (IYS) sutures (Yin and Harrison, 2000). To the south of the Indus–Yarlung suture is the Himalaya Mountains that consist of three tectonic belts; the Tethyan Himalaya (TH), High Himalaya (HH), and Low Himalaya (LH). The belts are separated, from north to south, by the north-dipping Main Central Thrust (MCT) and the Main Boundary Thrust (MBT) (Fig. 1).

The Lhasa terrane has a Mid-Proterozoic and Early Cambrian basement overlain by Ordovician–Triassic shallow marine clastic sediments. This terrane is commonly believed to be rifted apart from the Gondwanaland in Triassic or Mid-Late Jurassic time, then drifted northward, and finally collided with the Qiangtang terrane (Yin and Harrison, 2000). The crystalline basement within the Lhasa terrane crops out along the northern margin of the terrane as an orthogneiss (e.g., the Amdo orthogneiss) aged at 530 to 850 Ma (Guynn et al., 2006), whereas the Ordovician–Triassic strata mainly occur in both the northern and southern flanks of the terrane. The terrane has undergone a complex tectonic evolution, being affected, from south to north, by subduction of the Neo-Tethyan oceanic-slab in the Cretaceous (Chung et al., 2005) which produced the IYS, the Xigaze fore-arc basin (Durr, 1996), and the Andean-type Gangdese magmatic arc batholiths (120–70 Ma; Chu et al., 2006; Wang et al., 2008). The India–Eurasia collision initiated at around 65 Ma (Mo et al., 2003) and subsequent post-collision tectonic and magmatic activities have significantly thickened the Gangdese crust and resulted in widespread shallow granitic intrusions and crust deformation structures (Chung et al., 2005; Hou et al., 2006a, 2006b, 2006c; Mo et al., 2005). After closure of the Neo-Tethyan ocean, at least two episodes of magmatic activity (i.e., syn-collision, 65–38 Ma, and post-collision, 26–10 Ma) have been recognized in the Gangdese magmatic belt. The syn-collision magmatism produced granitoid batholiths of Paleocene age (66–55 Ma; Chu et al., 2006), the 5000-m-thick Linzizong volcanic succession (LVS) (65–43 Ma; Mo et al., 2003, 2007, 2008),

and the smaller volume Eocene Dazi picritic-basalt lavas (DPL) (40-38 Ma; Gao et al., 2008) (Fig. 1). These magmas formed in the context of northward subduction (Ding et al., 2003), a subsequent roll-back (Chung et al., 2005), and finally the break-off of the Neo-Tethyan oceanic slab (Gao et al., 2008). Post-collision magmatic activity produced Miocene potassic and ultrapotassic magmas (Miller et al., 1999; Turner et al., 1993; Williams et al., 2004; Zhao et al., 2009), and associated porphyritic granitoid stocks (Gao et al., 2010; Hou et al., 2004, 2009; Qu et al., 2009; Xu et al., 2010) that intruded into the Gangdese batholith and its volcanic-sedimentary sequence. Post-collision magmatism was controlled by a series of N–S-striking normal faults that transverse across the orogen (Hou et al., 2004), and dated between ~18 Ma and 13.5 Ma (Blisniuk et al., 2000).

A three-stage model was proposed to address tectono-magmatic evolution during the main India–Eurasia collision in Tibet (Hou et al., 2006a, 2006b, 2013; Mo et al., 2007) (Fig. 2). From ~70 to 60 Ma, roll-back of a near-flatly-subducted Neo-Tethyan oceanic-slab (Chung et al., 2005) facilitated the early dragging down of the attached Indian continental lithosphere and collision with the Eurasian continent, leading to initial shortening of the Eurasian continental crust and associated crustal anatexis. Paleocene granitoids were generated between ca. 66 and 58 Ma. Subsequently, the thermal structure of the mantle wedge was changed, resulting in generation of early LVS magmas at 65 ~ 60 Ma. From ~60 to 54 Ma, the slab roll-back mechanism was substituted by deep subduction of the Indian continental lithosphere, which most likely caused a sudden decreasing of convergent rate from 170 mm/a (at ~70–60 Ma) to 105 mm/a (at ~60–54 Ma) (Lee and Lawver, 1995). This resulted in the emplacement of crust-derived calc-alkaline granitoids in the eastern Gangdese belt at 54–52 Ma. At ~53–42 Ma, break-off of the Neo-Tethyan slab occurred at depth and upwelling of asthenosphere material through this “window” triggered partial melting of the lithospheric mantle, in turn generating numerous small gabbro intrusions (52 to 47 Ma) and tholeiitic subvolcanic rocks (42 Ma) along the Gangdese belt. Another direct consequence of slab break-off was the sudden decreasing of convergence rate from ~90 mm/a to ~60 mm/a at ~40 Ma (Lee and Lawver, 1995), as well as stress relaxation of the Lhasa terrane, during which abundant polymetallic mineralization took place.

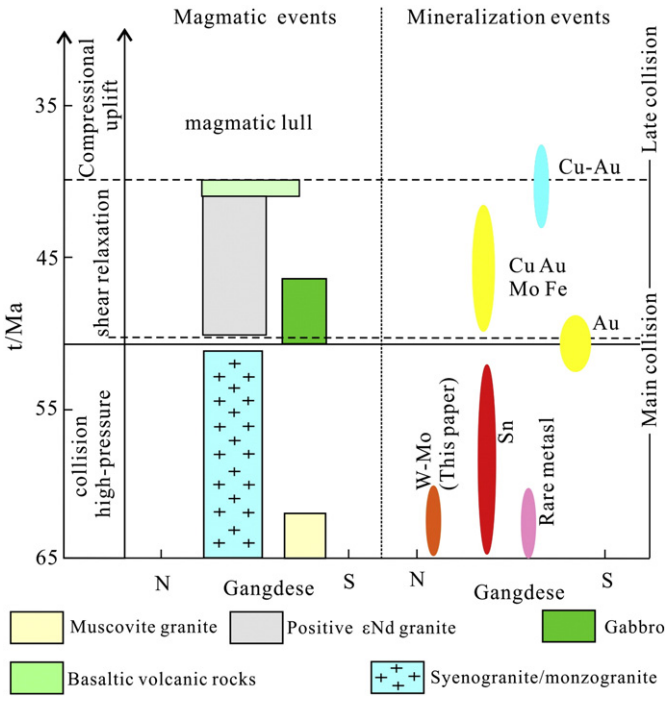

Fig. 2. Major tectonic, magmatic, and mineralization events during the India–Eurasia collision in Tibet.
Modified after (Hou et al., 2006a, 2006b, 2006c).

3. Geology of the Hahaigang deposit

The Hahaigang W–Mo polymetallic deposit is located in the western section of the Maizhokunggar–Jiali polymetallic belt which is part of the

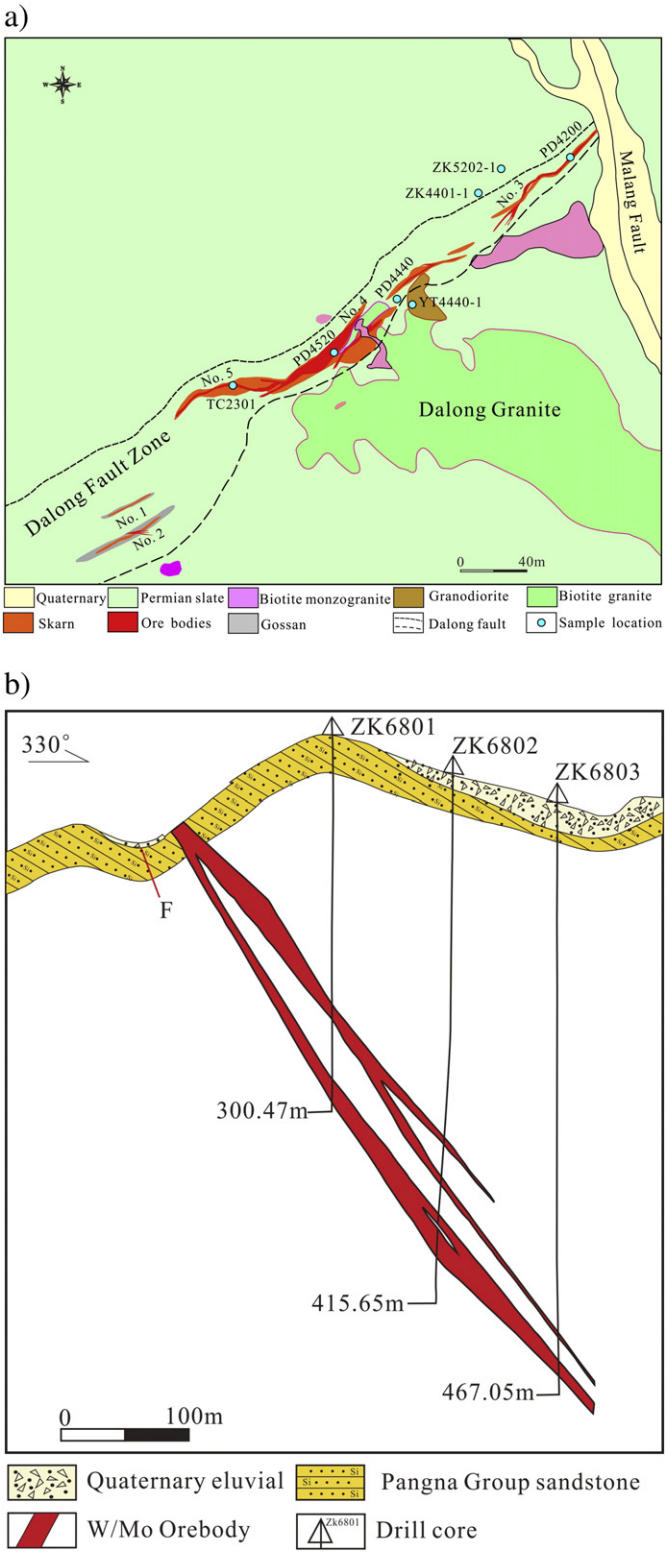

Fig. 3. Simplified geological map (a) and cross section (b) of Hahaigang W-Mo polymetallic deposit (modified after Guilin Research Institute of Geology for Mineral Resources, 2009).

Gangdese metallogenic belt, and 60 km south of the Namucuo–Jiali fault zone (Fig. 1). The fault zone is part of the E–W-striking Shiquanhe–Shenzha–Jiali fault zone (Hou et al., 2006c; Pan et al., 2006). It separates two tectonic units, the Anglonggangri–Bange–Tengchong magmatic belt in the north and the Lunggar–Gongbo'gyamda fault-block zone in the south.

The rocks exposed in the deposit and vicinity are predominantly quartz sandstone and slate of the Lower-Permian Pangna Group (Fig. 3). Early Cretaceous granite porphyry, Paleogene fine-grained biotite monzogranite, and biotite granodiorite occur mostly in the east of the deposit. Detailed descriptions of the granitoids are included in Section 4 of this paper.

The Dalong anticline is a major fold in the area. The anticline plunges southwest with a pitch angle at 10–15°. Its northwest limb is truncated by the northeast-striking Dalong fault zone. The fault zone extends at least 5.2 km in length and is 20–100 m wide. It dips toward the northwest at 55–70°. As shown in Fig. 3, the Dalong fault zone becomes wider towards the southwest. The fault zone shows a curved fault surface and local pinch and swelling structure. The fault zone is characterized by breccia, cataclasite, and foliated slate that exhibit silica, chloritic and pyritic alteration. The fault zone controls distribution of ore bodies of the Hahaigang deposit (Fig. 3). In the northeast, the zone is displaced by a younger NW-trending fault, the Malang fault.

Drilling, trenching, and testing shafts have identified five main skarn ore bodies in the Hahaigang deposit to date. The skarn ore bodies, hosted by quartz sandstone and slate of the Lower-Permian Pangna Group, occur within the Dalong fault zone. The No. 1 ore body is present as a chloritized skarn, and the other four ore bodies are within garnet skarn. No. 2, No, 3 and No. 4 are the main ore bodies in the deposit.

No. 2 ore body is present as a vein type. It is 240 m long horizontally, and extends up to 150 m in depth at a dip of 62–66° to 325°. Its thickness ranges from 1 m to 14 m with an average of 4.5 m. Ore minerals include sphalerite, galena, and chalcopyrite. No. 3 W–Mo ore body occurs as veins and lenses. It is 320 m long horizontally and extends up

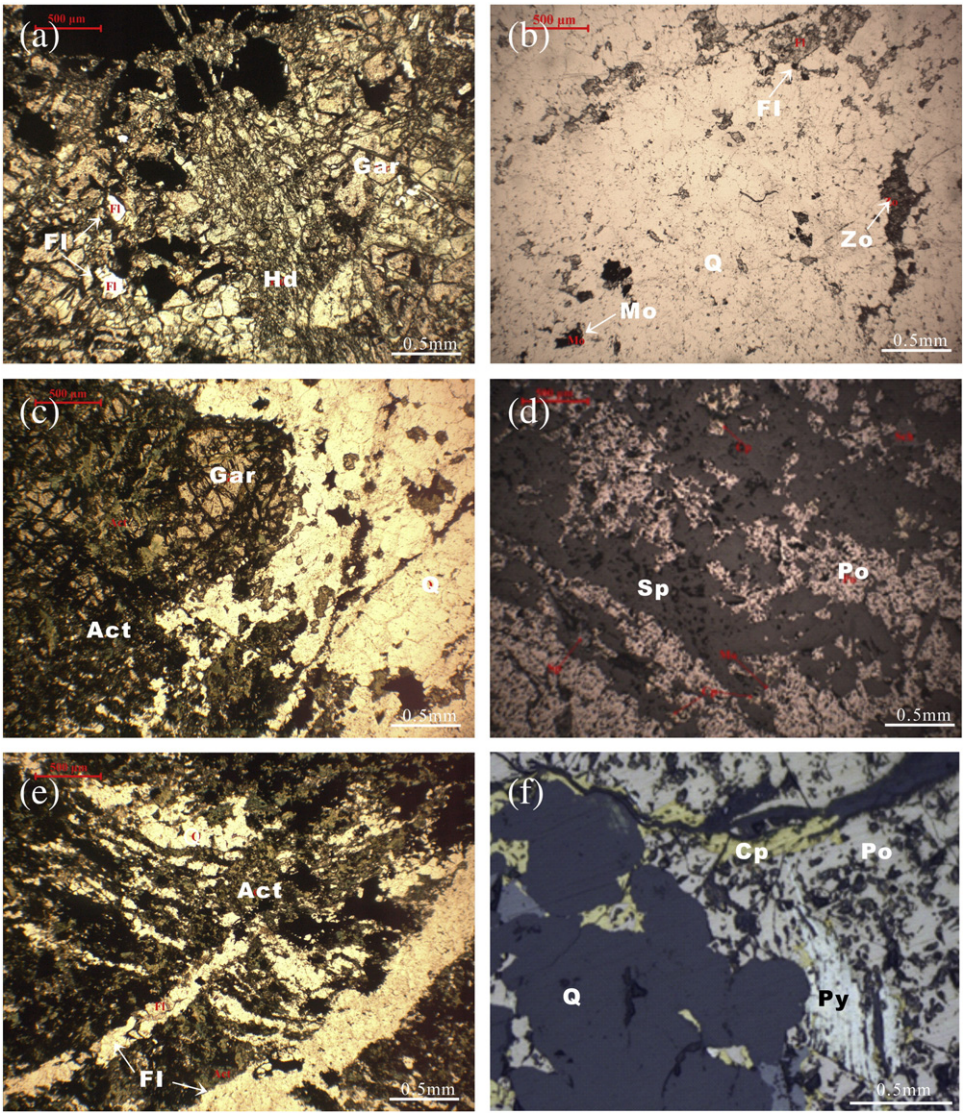

Fig. 4. Photomicrographs showing textures of skarn minerals, W–Mo ores, and ilvaite relationship to other skarn minerals and magmatic rocks. See text for detailed description. Abbreviations: Act = Actinolite, Bi = Biotite, Cp = Chalcopyrite, Di = Diopside, E-Ilv = Early ilvaite, Ep = Eposite, Fl = Fluorite, Gar = Garnet, Hd = Hedenbergite, Kf = Potassic feldspar, L-Ilv = Late ilvaite, Mo = Molybdenite, Ms = Muscovite, Mt = Magnetite, Pl = Plagioclase; Po = Pyrrhotite, Qz = Quartz, Sch = Scheellite, Zo = Zoisite. (a) Skarn minerals of garnet and hedenbergite which are overprinted by late fluorite in plane-polarized light. (b) Quartz vein consists of zoisite, fluorite, and molybdenite, in skarn in plane-polarized light. (c) Skarn mineral garnet altered to actinolite by late hydrothermal activity in plane-polarized light. (d) Metallic minerals in skarn ore bodies in reflected light. (e) Actinolite is truncated by late fluorite vein in plane-polarized light. (f) Early euhedral pyrite showing shear deformation in reflected light. (g) Backscattered electron (BSE) image of scheelite and molybdenite solid solution texture. (h) Ore assemblage of chalcopyrite, pyrrhotite, ilvaite, and magnetite in reflected light. (i) Ilvaite vein cross-cutting diopside in plane-polarized light. (g) Granite porphyry showing brittle-ductile deformation structure in cross-polarized light. (k) Granodiorite texture (sample YT4440-1) in cross-polarized light. (l) Biotite monzogranite texture in cross-polarized light (sample ZK4401-1).

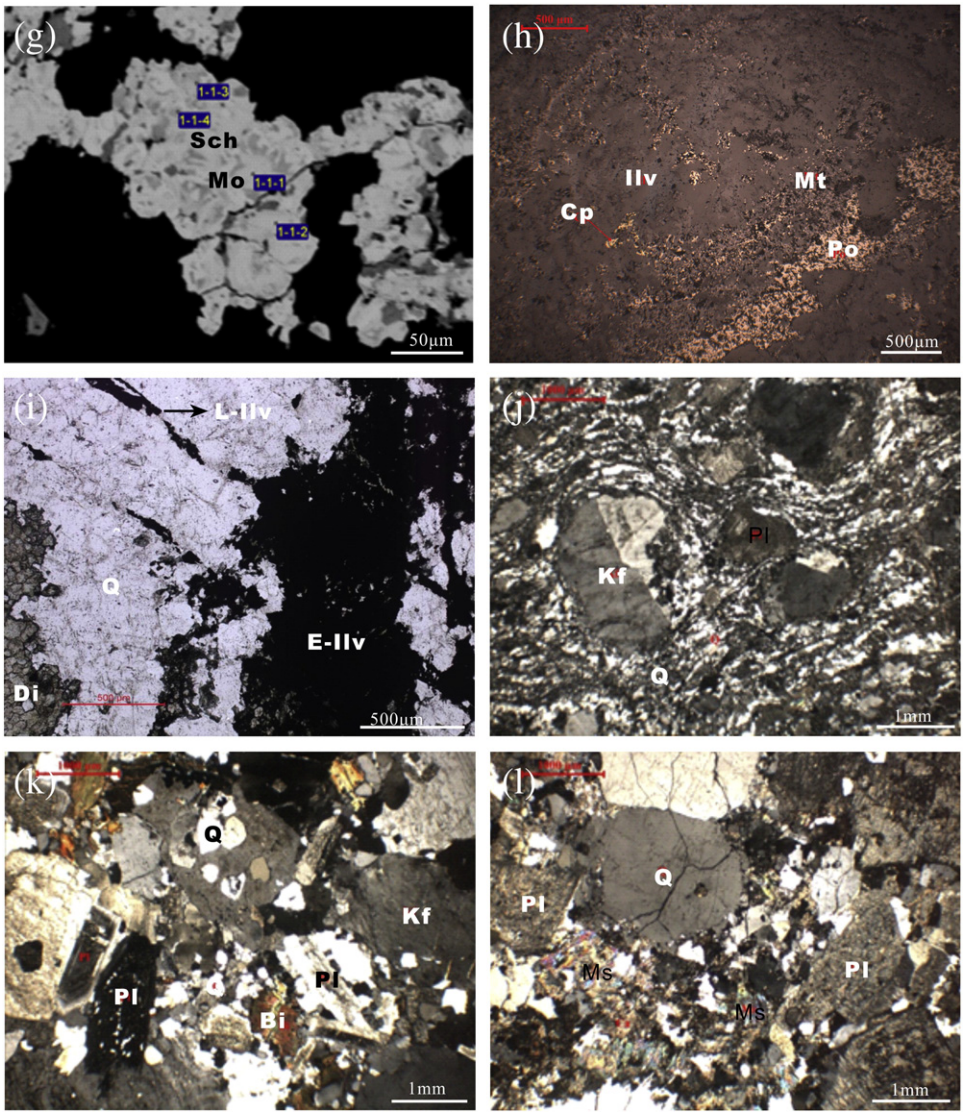

Fig. 4 (*continued*).

to 400 m deep at a dip of 55–60° to 310–325°. Its thickness ranges between 1.11 m and 16.94 m with an average thickness of 5.91 m. Its ore minerals include scheelite and molybdenite, with an average grade of 0.2% WO_3. The No. 4 W–Mo ore body is a vein and disseminated type. It is 800 m long horizontally and extends up to 500 m deep at a dip of 58–72° to 300–327°. Its thickness ranges between 1 m and 78 m with an average thickness of 26.4 m. Scheelite is the main ore mineral, giving the orebody an average grade of 0.2% WO_3. The gangue minerals include quartz, fluorite, garnet, chlorite, and diopside. The No. 4 ore body is displaced by a granodiorite intrusion.

Intensive drilling has also revealed a vertical metal zoning pattern. For example, the No. 2 Cu–Pb–Zn ore body occurs at the 4800–5000 m level (above sea level), the No. 5 W ore body at 4850–4480 m, the No. 4 W–Mo ore body at 4620–4100 m, and the No. 3 W–Mo ore body at 4360–3720 m (Guilin Research Institute of Geology for Mineral Resources, 2009). On horizontal level, the Cu–Pb–Zn, W–Mo, and Mo ore bodies all occur within the skarn zone. The skarns show silica, garnet and pyrrhotite alteration, and are overprinted by later carbonatization. The No. 5 ore body occurs in the center of the deposit. A sequence of mineralization types occurs around the center to form a horizontal zonation pattern. For example, the center is dominated by massive W–Mo mineralization, outward from the center the sequence changes to vein-type W–Mo, veinlet-stockwork Cu–Pb–Zn-bearing W, stockwork-disseminated Pb–Zn, and vein-type Cu–Pb–Zn.

Two stages of polymetallic mineralization are recorded in the Hahaigang deposit. The first stage, comprise W–Mo mineralization which began with a prograde skarn assemblage of water-free minerals, such as garnet and pyroxene (Fig. 4a), with a small amount of quartz veinlets and disseminated white scheelite, molybdenite, and magnetite (Fig. 4b). It was immediately followed by formation of a large volume of retrograde stage skarn with hydrous silicate minerals (e.g., chlorite, epidote, hornblende, and sericite) (Fig. 4c) and deposition of metallic minerals scheelite, magnetite, pyrrhotite, and molybdenite. The second, later stage was of Cu–Pb–Zn quartz-sulfide mineralization stage which started with formation of pyrite and sulfide ore minerals chalcopyrite, sphalerite, and galena (Fig. 4d), followed by formation of small amounts of galena, bismuth, and native bismuth that occur as veinlets. Large amounts of gangue minerals, including chlorite and fluorite, occur as alteration products at the end of this stage (Fig. 4e).

Both pyrite and chalcopyrite occur in two generations. Optical microscopy shows first-generation euhedral pyrite with shear deformation structures (Fig. 4f), whereas the second-generation pyrite occurs as veinlets. The first-generation chalcopyrite is disseminated and coexists with pyrrhotite and sphalerite. Both chalcopyrite and pyrrhotite

Table 1
Zircon LA–ICP–MS U–Pb data of the igneous rocks in Hahaigang W–Mo deposit.

Spots	Th/U	Isotope ratios				Isotopic ratios: (1σ)				Age estimates (Ma)				Age estimates: (1σ)			
		Pb^{207}/Pb^{206}	Pb^{206}/U^{238}	Pb^{207}/U^{235}	Pb^{208}/Th^{232}	Pb^{207}/Pb^{206}	Pb^{206}/U^{238}	Pb^{207}/U^{235}	Pb^{208}/Th^{232}	Pb^{207}/Pb^{206}	Pb^{206}/U^{238}	Pb^{207}/U^{235}	Pb^{208}/Th^{232}	Pb^{207}/Pb^{206}	Pb^{206}/U^{238}	Pb^{207}/U^{235}	Pb^{208}/Th^{232}
Sample: ZK5202-1																	
ZK5202-1_1	0.25	0.05171	0.0193	0.14132	0.00335	0.00107	0.00039	0.00296	0.00007	272.7	123.2	134.2	67.7	46.78	2.44	2.63	1.39
ZK5202-1_2	0.86	0.05487	0.01402	0.11252	0.00067	0.0011	0.00028	0.00226	0.00001	407.1	89.7	108.3	13.5	43.84	1.77	2.06	0.26
ZK5202-1_3	0.15	0.05081	0.01738	0.12793	0.00588	0.00109	0.00035	0.00279	0.00013	232.3	111.1	122.2	118.4	48.92	2.21	2.51	2.56
ZK5202-1_4	3.19	0.04924	0.01825	0.122	0.00529	0.00127	0.00037	0.00324	0.0001	159.4	116.6	116.9	106.6	59.29	2.37	2.93	2.06
ZK5202-1_5	1.03	0.0573	0.0192	0.15239	0.00648	0.00194	0.00042	0.00545	0.00015	502.4	122.6	144	130.5	73.42	2.64	4.8	3.08
ZK5202-1_6	0.86	0.04823	0.01851	0.12515	0.00587	0.0013	0.00038	0.00349	0.00013	110.5	118.3	119.7	118.4	62.55	2.42	3.15	2.52
ZK5202-1_7	0.85	0.0502	0.01758	0.12542	0.00524	0.00106	0.00035	0.00269	0.0001	204.3	112.4	120	105.7	48.48	2.23	2.43	2.03
ZK5202-1_8	0.22	0.04845	0.01802	0.12434	0.00559	0.00101	0.00036	0.00262	0.00011	121.5	115.2	119	112.7	48.43	2.28	2.36	2.26
ZK5202-1_9	0.47	0.05301	0.01707	0.12861	0.00606	0.00116	0.00034	0.00285	0.00012	329.4	109.1	122.8	122	48.74	2.17	2.57	2.43
ZK5202-1_10	0.89	0.05399	0.01734	0.13328	0.00549	0.00114	0.00035	0.00286	0.00011	370.3	110.8	127	110.6	47.09	2.2	2.56	2.12
ZK5202-1_11	0.30	0.07052	0.01685	0.17016	0.0058	0.00142	0.00034	0.00343	0.00011	943.6	107.7	159.6	116.8	40.6	2.13	2.98	2.22
ZK5202-1_12	1.84	0.05767	0.01693	0.13569	0.00525	0.0015	0.00035	0.00364	0.00011	516.9	108.2	129.2	105.8	56.43	2.21	3.25	2.11
ZK5202-1_13	0.60	0.06232	0.01625	0.14349	0.00567	0.0013	0.00032	0.00302	0.00011	685.1	103.9	136.1	114.2	43.87	2.06	2.68	2.2
ZK5202-1_14	0.37	0.05447	0.01661	0.13164	0.00575	0.00119	0.00033	0.00292	0.00012	390.6	106.2	125.6	115.9	48.13	2.12	2.62	2.35
ZK5202-1_15	1.02	0.05294	0.01605	0.12147	0.00529	0.00123	0.00032	0.00287	0.0001	326.2	102.7	116.4	106.7	51.67	2.06	2.6	2.11
ZK5202-1_16	0.39	0.05426	0.0155	0.11953	0.00504	0.00111	0.00031	0.00246	0.0001	381.6	99.2	114.6	101.7	45.19	1.96	2.23	1.95
ZK5202-1_17	0.34	0.05576	0.01524	0.12076	0.00345	0.00113	0.0003	0.00246	0.00007	442.5	97.5	115.8	69.6	44.09	1.93	2.23	1.34
ZK5202-1_18	0.43	0.05058	0.01801	0.131	0.00604	0.00119	0.00036	0.00315	0.00013	221.8	115	125	121.7	53.44	2.31	2.82	2.57
ZK5202-1_19	0.12	0.05064	0.01796	0.13366	0.00632	0.00116	0.00036	0.00313	0.00016	224.5	114.7	127.4	127.3	52.15	2.29	2.8	3.17
ZK5202-1_20	0.48	0.0483	0.01792	0.12307	0.00553	0.00099	0.00036	0.00255	0.00011	113.8	114.5	117.8	111.5	47.87	2.26	2.31	2.14
ZK5202-1_21	1.21	0.05424	0.01642	0.12698	0.00532	0.00223	0.00037	0.00547	0.00014	380.9	105	121.4	107.3	89.21	2.37	4.92	2.74
ZK5202-1_22	0.24	0.06988	0.01623	0.16438	0.00853	0.00156	0.00033	0.00373	0.00018	924.9	103.8	154.5	171.6	45.13	2.08	3.26	3.62
ZK5202-1_23	0.42	0.04874	0.01688	0.1173	0.00501	0.00105	0.00034	0.00256	0.0001	135.4	107.9	112.6	101	49.95	2.14	2.33	2.02
ZK5202-1_24	0.57	0.0491	0.01965	0.13694	0.00569	0.00104	0.00039	0.00292	0.00011	152.4	125.4	130.3	114.6	48.69	2.48	2.61	2.23
ZK5202-1_25	0.20	0.05192	0.01621	0.12336	0.00506	0.00109	0.00032	0.00263	0.0001	281.9	103.6	118.1	101.9	47.5	2.06	2.37	2.1
Sample: ZK4401-1																	
ZK4401-1_1	0.42	0.05403	0.00834	0.06122	0.00287	0.00138	0.00017	0.00157	0.00006	372.1	53.6	60.3	57.9	56.38	1.09	1.5	1.3
ZK4401-1_2	0.49	0.04818	0.00905	0.05999	0.00271	0.001	0.00018	0.00125	0.00005	108	58.1	59.2	54.7	48.07	1.15	1.19	1.04
ZK4401-1_3	0.45	0.0478	0.0091	0.0606	0.00281	0.00098	0.00018	0.00125	0.00005	88.2	58.4	59.7	56.7	48.78	1.16	1.19	1.07
ZK4401-1_4	0.42	0.0472	0.00923	0.06201	0.00287	0.00098	0.00018	0.0013	0.00005	59.1	59.2	61.1	57.9	49.43	1.17	1.24	1.11
ZK4401-1_5	0.36	0.04759	0.00911	0.06164	0.00287	0.001	0.00018	0.0013	0.00006	77.9	58.4	60.7	58	49.83	1.16	1.24	1.12
ZK4401-1_6	0.43	0.04806	0.00889	0.05991	0.00274	0.00113	0.00018	0.00141	0.00006	102.5	57	59.1	55.4	54.6	1.14	1.36	1.16
ZK4401-1_7	0.49	0.04636	0.00853	0.05681	0.00264	0.00137	0.00018	0.00169	0.00006	16.2	54.8	56.1	53.3	68.69	1.13	1.63	1.29
ZK4401-1_8	0.30	0.0471	0.00884	0.05943	0.00295	0.00109	0.00018	0.00139	0.00006	54	56.7	58.6	59.6	54.87	1.14	1.33	1.27
ZK4401-1_9	0.38	0.04604	0.00907	0.05871	0.00267	0.00129	0.00019	0.00166	0.00007	0.1	58.2	57.9	53.9	65.4	1.2	1.59	1.34
ZK4401-1_10	0.50	0.04648	0.0089	0.05837	0.00271	0.00107	0.00018	0.00134	0.00005	22.5	57.1	57.6	54.7	53.44	1.14	1.29	1.1
ZK4401-1_11	0.45	0.04776	0.00912	0.06026	0.00279	0.00102	0.00018	0.00129	0.00005	86.6	58.5	59.4	56.3	50.62	1.16	1.23	1.09
ZK4401-1_12	0.30	0.04787	0.00875	0.05966	0.00286	0.00105	0.00017	0.00131	0.00006	91.8	56.2	58.8	57.8	52.19	1.12	1.26	1.17
ZK4401-1_13	0.24	0.04948	0.00845	0.06003	0.00295	0.00108	0.00017	0.00132	0.00006	170.7	54.3	59.2	59.6	50.17	1.08	1.26	1.23
ZK4401-1_14	0.24	0.05069	0.00872	0.06095	0.00291	0.00107	0.00017	0.00129	0.00006	226.8	56	60.1	58.7	48.01	1.11	1.23	1.16
ZK4401-1_15	0.42	0.04716	0.00907	0.06124	0.0029	0.00103	0.00018	0.00135	0.00006	56.7	58.2	60.4	58.5	51.79	1.16	1.29	1.15
ZK4401-1_16	0.44	0.04704	0.00905	0.06005	0.00283	0.00101	0.00018	0.0013	0.00006	50.8	58.1	59.2	57.2	50.88	1.15	1.24	1.11
ZK4401-1_17	0.34	0.05792	0.00808	0.06651	0.00322	0.00144	0.00016	0.00166	0.00007	526.3	51.9	65.4	64.9	53.92	1.05	1.58	1.45
ZK4401-1_18	0.53	0.04751	0.0089	0.06029	0.00273	0.00107	0.00018	0.00136	0.00005	74.1	57.1	59.4	55.2	53.36	1.14	1.3	1.1

ZK4401-1_19	0.56	0.0517	0.00922	0.06723	0.00313	0.00116	0.00018	0.00151	0.00006	272.3	59.1	66.1	63.2	50.52	1.18	1.44	1.24
ZK4401-1_20	0.39	0.04787	0.00906	0.06078	0.00291	0.001	0.00018	0.00127	0.00006	91.9	58.1	59.9	58.6	49.74	1.15	1.22	1.12
ZK4401-1_21	0.26	0.04725	0.00863	0.05811	0.00274	0.00114	0.00017	0.00141	0.00006	61.4	55.4	57.4	55.3	57.07	1.11	1.35	1.27
ZK4401-1_22	0.53	0.04876	0.00868	0.06036	0.00277	0.00111	0.00017	0.00138	0.00006	136.3	55.7	59.5	55.9	52.77	1.11	1.32	1.12
ZK4401-1_23	0.40	0.04875	0.0088	0.06111	0.00285	0.00107	0.00018	0.00135	0.00006	135.8	56.5	60.2	57.5	50.87	1.12	1.29	1.14
ZK4401-1_24	0.17	0.04964	0.00864	0.06052	0.00304	0.00104	0.00017	0.00127	0.00006	178	55.5	59.7	61.4	47.98	1.1	1.21	1.23
ZK4401-1_25	0.60	0.05025	0.00921	0.06693	0.00288	0.00108	0.00018	0.00145	0.00006	206.7	59.1	65.8	58.1	49.28	1.17	1.38	1.12
ZK4401-1_26	0.51	0.04734	0.00903	0.0594	0.00273	0.00108	0.00018	0.00136	0.00005	66	58	58.6	55.1	53.97	1.15	1.3	1.11
ZK4401-1_27	0.32	0.04733	0.00887	0.06027	0.00286	0.00104	0.00018	0.00132	0.00006	65.3	56.9	59.4	57.8	51.82	1.13	1.27	1.16
ZK4401-1_28	0.43	0.04707	0.00907	0.06119	0.00294	0.00112	0.00018	0.00146	0.00006	52.6	58.2	60.3	59.4	56.2	1.17	1.4	1.24
ZK4401-1_29	0.45	0.0503	0.00861	0.06057	0.00272	0.00113	0.00017	0.00136	0.00005	209	55.2	59.7	55	51.07	1.1	1.3	1.1
ZK4401-1_30	0.59	0.04643	0.00892	0.05812	0.00272	0.00108	0.00018	0.00136	0.00005	20	57.2	57.4	54.8	54.27	1.14	1.3	1.1
ZK4401-1_31	0.85	0.04947	0.00876	0.05695	0.00272	0.00213	0.0002	0.00246	0.00008	170.2	56.2	56.2	54.9	97.43	1.27	2.36	1.55
ZK4401-1_32	0.44	0.0479	0.00918	0.06236	0.00291	0.00102	0.00018	0.00133	0.00006	93.2	58.9	61.4	58.7	50.69	1.16	1.27	1.13
ZK4401-1_33	0.59	0.05076	0.00879	0.062	0.00286	0.00127	0.00018	0.00156	0.00006	229.8	56.4	61.1	57.8	56.76	1.14	1.49	1.22
ZK4401-1_34	0.48	0.04738	0.00896	0.06026	0.00286	0.00097	0.00018	0.00123	0.00005	68	57.5	59.4	57.7	48.51	1.13	1.18	1.08
ZK4401-1_35	0.45	0.04674	0.00875	0.05941	0.00268	0.00106	0.00017	0.00134	0.00005	35.9	56.1	58.6	54.1	52.37	1.12	1.29	1.09
Sample: YT4440																	
YT-4440_1	0.43	0.04648	0.00965	0.0634	0.00304	0.001	0.00019	0.00137	0.00006	22.6	61.9	62.4	61.4	50.27	1.23	1.31	1.2
YT-4440_2	0.45	0.05543	0.00896	0.07162	0.00318	0.00117	0.00018	0.00152	0.00006	429.3	57.5	70.2	64.2	45.94	1.14	1.44	1.24
YT-4440_3	0.53	0.04934	0.01114	0.07671	0.00316	0.00119	0.00023	0.00187	0.00007	163.9	71.4	75.1	63.8	55.39	1.44	1.76	1.35
YT-4440_4	0.51	0.04763	0.00899	0.06101	0.00282	0.0012	0.00018	0.00155	0.00006	80.1	57.7	60.1	57	59.66	1.17	1.48	1.23
YT-4440_5	0.24	0.0474	0.00877	0.05977	0.00303	0.00101	0.00018	0.00128	0.00006	69	56.3	58.9	61.3	50.52	1.12	1.22	1.23
YT-4440_6	0.71	0.0476	0.00931	0.06256	0.00283	0.00099	0.00019	0.00131	0.00005	78.7	59.8	61.6	57.1	49.59	1.19	1.25	1.08
YT-4440_7	0.46	0.2065	0.00847	0.24899	0.00965	0.00414	0.00017	0.00501	0.00018	2878.3	54.4	225.8	194	32.19	1.08	4.07	3.61
YT-4440_8	0.22	0.19646	0.00698	0.19634	0.01343	0.00393	0.00014	0.00394	0.00025	2797	44.8	182	269.6	32.33	0.89	3.34	5
YT-4440_9	0.67	0.04678	0.00841	0.05579	0.00254	0.00107	0.00017	0.00128	0.00005	38	54	55.1	51.4	52.94	1.08	1.23	1.02
YT-4440_10	0.36	0.04595	0.00932	0.06082	0.00299	0.00118	0.00019	0.00158	0.00007	0.1	59.8	60	60.4	55.49	1.22	1.51	1.39
YT-4440_11	0.28	0.05069	0.00815	0.06094	0.00298	0.00113	0.00016	0.00137	0.00006	226.8	52.3	60.1	60.1	50.77	1.05	1.31	1.25
YT-4440_12	0.52	0.05167	0.00911	0.06503	0.00287	0.00173	0.0002	0.0022	0.00008	270.7	58.5	64	57.8	75.07	1.25	2.1	1.57
YT-4440_13	0.44	0.04998	0.00865	0.06021	0.00274	0.00107	0.00017	0.00129	0.00005	193.9	55.5	59.4	55.2	48.84	1.11	1.23	1.08
YT-4440_14	0.45	0.04684	0.00892	0.05923	0.00267	0.00101	0.00018	0.00129	0.00005	40.9	57.3	58.4	53.9	50.1	1.14	1.23	1.06
YT-4440_15	0.50	0.04796	0.01048	0.06963	0.00297	0.00149	0.00022	0.00218	0.00008	96.2	67.2	68.3	59.9	72.86	1.41	2.07	1.56
YT-4440_16	0.29	0.10162	0.16809	2.35123	0.05842	0.00203	0.00335	0.04901	0.00111	1654	1001.6	1227.9	1147.7	36.55	18.46	14.85	21.15
YT-4440_17	0.40	0.04713	0.00934	0.06381	0.00293	0.00099	0.00019	0.00135	0.00006	55.4	59.9	62.8	59.2	49.84	1.19	1.29	1.15
YT-4440_18	0.46	0.04797	0.00888	0.0622	0.00294	0.00102	0.00018	0.00133	0.00006	96.4	57	61.3	59.4	50.74	1.13	1.27	1.15
YT-4440_19	0.29	0.0504	0.00758	0.05464	0.0024	0.00116	0.00015	0.00126	0.00005	213.3	48.7	54	48.5	52.57	0.98	1.22	1.06
YT-4440_20	0.75	0.04812	0.00933	0.06454	0.00298	0.00108	0.00019	0.00146	0.00006	105.3	59.9	63.5	60.1	52.14	1.2	1.39	1.18
YT-4440_21	0.38	0.0475	0.00898	0.06188	0.00289	0.00099	0.00018	0.0013	0.00006	73.6	57.7	61	58.3	49.53	1.15	1.24	1.13
YT-4440_22	0.45	0.04719	0.00872	0.06001	0.00281	0.00103	0.00017	0.00131	0.00006	58.6	56	59.2	56.7	51.54	1.12	1.26	1.12
YT-4440_23	0.67	0.05018	0.0109	0.07529	0.00352	0.00152	0.00023	0.00231	0.00008	203.5	69.9	73.7	71.1	68.71	1.46	2.18	1.67
YT-4440_24	0.39	0.0543	0.00823	0.06515	0.00297	0.00115	0.00016	0.00138	0.00006	383.4	52.8	64.1	59.9	46.62	1.05	1.32	1.17
YT-4440_25	0.54	0.04864	0.00862	0.06074	0.0028	0.00108	0.00017	0.00135	0.00006	130.6	55.3	59.9	56.6	51.22	1.11	1.29	1.12
YT-4440_26	0.41	0.04904	0.00863	0.06053	0.00274	0.00102	0.00017	0.00127	0.00005	149.9	55.4	59.7	55.3	48.09	1.1	1.21	1.07
YT-4440_27	0.35	0.04702	0.00803	0.0542	0.00256	0.0011	0.00016	0.00128	0.00006	50.1	51.6	53.6	51.7	55.37	1.04	1.23	1.11
YT-4440_28	0.54	0.0479	0.00809	0.05489	0.00238	0.00099	0.00016	0.00114	0.00005	93.3	51.9	54.3	48	49.35	1.03	1.1	0.92
YT-4440_29	0.35	0.0468	0.00845	0.05828	0.00272	0.00111	0.00017	0.00139	0.00006	38.8	54.2	57.5	54.9	55.06	1.09	1.34	1.19
YT-4440_30	0.56	0.05287	0.00649	0.04858	0.00182	0.00111	0.00013	0.00102	0.00004	323.3	41.7	48.2	36.7	46.91	0.83	0.99	0.71
YT-4440_31	0.49	0.05283	0.0086	0.06691	0.00312	0.00124	0.00017	0.00158	0.00006	321.6	55.2	65.8	62.9	52.26	1.11	1.5	1.3
YT-4440_32	0.65	0.04687	0.00835	0.05597	0.00257	0.00114	0.00017	0.00137	0.00005	42.6	53.6	55.3	51.9	56.26	1.08	1.32	1.07
YT-4440_33	0.75	0.0475	0.00901	0.06081	0.00273	0.00106	0.00018	0.00136	0.00005	73.8	57.8	59.9	55	52.72	1.16	1.3	1.08
YT-4440_34	0.52	0.04975	0.00868	0.06161	0.00276	0.00116	0.00018	0.00144	0.00006	183.5	55.7	60.7	55.6	53.3	1.12	1.38	1.15
YT-4440_35	0.74	0.04755	0.00867	0.05888	0.00262	0.0011	0.00017	0.00137	0.00005	76.2	55.6	58.1	52.9	54.92	1.12	1.32	1.06

grains share common grain boundaries with smooth contacts to each other; and sphalerite and pyrrhotite demonstrate exsolution texture. The second-generation chalcopyrite occurs as veinlets. Scheelite and molybdenite locally occur as solid solution (Fig. 4g).

In addition to the skarn minerals diopside and actinolite, ilvaite has been observed as a skarn mineral in the deposit. It occurs as veins that cross-cut diopside and actinolite. It is also associated with magnetite, pyrrhotite, and chalcopyrite (Fig. 4h). Two generations of ilvaite are identified; the second-generation ilvaite veins may cross-cut the first-generation ilvaite (Fig. 4i).

4. Sampling and analytical methods

4.1. Sample descriptions

Molybdenite grains were selected from skarn ore samples that were collected from exploration shafts at the 4520-m and 4200-m levels, and from No. 2301 drill core. These ores include garnet, diopside, ilvaite, actinolite, chlorite, fluorite, scheelite, molybdenite, magnetite, and pyrrhotite. Ilvaite samples (HHG-5 and HHG-8) were collected from ore samples at the 4200-m level of an exploration shaft. Zircons of ZK 520101 and ZK4401-1 were selected from biotite monzogranite and granite porphyry collected in drill cores (Fig. 3) and the zircon YT4440-1 was selected from granodiorite at outcrops.

4.1.1. Sample ZK5202-1 mylonitized granite porphyry

This sample shows a mylonitization texture. The porphyroclasts are perthite, orthoclase, plagioclase, and minor muscovite (<1%). Some orthoclase (potassium feldspar) shows imbricated structure with slight kaolinization. Plagioclase feldspars may be altered by sericitization. Some muscovite flakes develop "mica fish" texture due to ductile shearing. The mylonitic foliation is defined by alignment of the porphyroclasts. The groundmass consists of quartz grains formed by dynamic recrystallization (45%) and by static recrystallization, and minor amount of fragments of feldspar, sericite, and calcite. Accessary minerals include apatite and zircon are not deformed. The mylonitized granite porphyry is superimposed by brittle fractures (Fig. 4j).

4.1.2. Sample YT4440-1 fine- and medium-grained granodiorite

This sample contains plagioclase feldspar (54–64%), quartz (26–36%), and orthoclase (3–4%). Minor apatite (<1%), magnetite (<1%), zircon (<1%), chalcopyrite (<1%), and pyrite (<1%) are also observed in the sample. Orthoclase is present as semi-euhedral or anhedral potassium feldspar and perthite in sizes between 0.2–5 mm. Semi-euhedral plagioclase feldspar grains are 0.2–3 mm long and 0.15–3 mm wide, showing slight alteration to sericite, carbonate and zoisite. Anhedral quartz grains are 0.2–5 mm, showing undulatory extinction. Hornblende is not observed in the sample; it may be replaced by biotite. Biotite flakes are of 0.2–1.5 mm, and some of them are replaced by chlorite and sphene. Biotite shows minor exsoluted magnetite and rutile (Fig. 4k).

4.1.3. Sample ZK4401-1 fine-grained biotite monzogranite

This sample consists of potassium feldspar (42–47%), plagioclase feldspar (25–30%), quartz (24–25%), biotite (3–4%), and minor apatite, orthite, magnetite, and pyrrhotite. Anhedral potassium feldspar grains range in size between 0.2 and 1 mm with slight kaolinization. Semi-euhedral plagioclase feldspar grains are 0.3–5 mm long and 0.2–3 mm wide; some of them are sericitized. Anhedral quartz grains are 0.2–5 mm. Biotite flakes are 0.2–1.5 mm, showing pseudoforms, replacement of muscovite and carbonate, and exsoluted rutile (Fig. 4l).

4.1.4. Sample HHG-5 diopside-skarn

This sample has a porphyroblastic texture. The minerals include diopside (78–79%), ilvaite (10–15%), actinolite (2–3%), magnetite (<1%), pyrrhotite (<1%), pyrite (<1%), and quartz (5–10%) (Fig. 4i). Anhedral magnetite grains coexist with ilvaite as veinlets that truncate diopside. Anhedral pyrrhotite and chalcopyrite occur as disseminated within diopside. Diopside occurs as short prisms and some of them are altered into actinolite. Ilvaite is prismatic or equant with its size ranging between 0.1 and 1.5 mm. It occurs as veinlets that cross-cut diopside and quartz interstitials (Fig. 4i). Fibrous actinolite crystals are found within diopside grains and ilvaite.

4.1.5. Sample HHG-8 pyrrhotite-bearing chalcopyrite ore

Major ore minerals seen in this sample are magnetite (4–5%), pyrrhotite (5–6%), chalcopyrite (2–3%), and molybdenite (<1%) (Fig. 4h). Gangue minerals include actinolite and quartz (69–74%), garnet (5–10%), diopside (4–5%), ilvaite (1–2%), and fluorite (1–2%). Ore minerals occur as anhedral grains, or as veinlets or disseminated within gangue minerals, and locally, the ore mineral veinlets cross cut quartz veins. Anhedral magnetite grains are 0.01–0.3 mm in filling grain boundary of gangue minerals, and they could be also filled by pyrrhotite and chalcopyrite. Anhedral pyrrhotite grains vary in size between 0.01 and 0.3 mm and also occupy the interstices between gangue minerals as veinlets or dissemination with magnetite. Disseminated anhedral chalcopyrite grains range between 0.01 and 0.3 mm and share common grain boundaries with pyrrhotite grains with smooth contacts. Molybdenite occurs as small flakes and is disseminated with the gangue minerals (mostly quartz grains). Diopside may occur as fillings within garnet, showing that the garnet crystallized earlier than the diopside. Both are partially replaced by actinolite with fluorite fillings as well (Fig. 4c, e). Quartz occurs as the youngest phase as it fills within other minerals. Some ilvaite grains occur along micro-fractures within gangue minerals.

4.2. Zircon LA–ICP–MS U–Pb analysis

Samples selected to isolate zircon grains were crushed and ground to produce fragments smaller than 0.2 mm. Manual heavy liquid rinsing and gravity method were used to select zircon grains before using a binocular microscope to hand-pick pure zircon grains. The zircon grains were analyzed by a laser ablation inductively coupled plasma mass spectrometry (LA–ICP–MS) at the Institute of Mineral Resources, Chinese Academy of Geological Sciences, Beijing. During preparation, zircon crystals were mounted in epoxy resin together with a standard zircon sample (of 417 Ma). The sample was then polished to get a cross-section through the grains to expose the central sections of zircon crystals. After polishing, cathodoluminescence (CL) and optical microphotography techniques were used to examine and analyze the morphology, zoning characteristics, and interior structure of each zircon grain. Zircon grains that met requirement for geochronological analysis were finally selected. The mount was then cleaned and gold-coated in preparation for analysis. The analytical procedure and methods, as well as data processing methods, follow Jian et al. (2003).

4.3. Molybdenite Re–Os analysis

An XRD analysis was conducted to examine molybdenite polymorphism and impurities before the Re–Os geochronological analysis method was applied. The Re–Os analysis work was conducted at the Institute of Geochemistry of the Chinese Academy of Science, Guiyang. The analytical procedure and methods, as well as data processing methods follow Du et al. (1994, 2001).

4.4. Ilvaite microprobe analysis

Selected through detailed petrographic observations, ilvaite and garnet grains were studied by microprobe analysis, conducted in the Microprobe Laboratory at the Institute of Mineral Resources, Chinese Academy of Geological Sciences, Beijing. Their chemical compositions were obtained by using JOEL-8230 electronic microprobe with an accelerating voltage of 20 kV, a beam diameter of 6 μm, a beam current of

34 nA, and peak and background counting times of 10 s. LiF, PET, and TAP crystal spectrometers were used for wavelength dispersive analyses. Standards used in the analyses are: albite for Na, diopside for Ca and Si, kyanite for Al, forsterite for Mg, fayalite for Fe, orthoclase for K, sphene for Ti, and spessartine for Mn. ZAF corrections were applied to all data.

5. Results of analyses

5.1. Zircon LA–ICP–MS geochronology

Table 1 shows LA–ICP–MS results for zircon grains selected from samples ZK5202-1, Zk4401-1, and YT4440. As shown in Table 1, there is a total of 25 zircon grains and 25 spots analyzed for sample ZK5202-1 of mylonitized granite porphyry. Among the 25 zircon grains, 16 yielded a $^{206}Pb/^{238}U$–$^{207}Pb/^{238}U$ concordia age of 109.1 ± 8.9 Ma (n = 16, MSWD = 2.6), and 16 spots yielded a weighted mean $^{206}Pb/^{238}U$ age of 114.0 ± 2.6 Ma (n = 16, MSWD = 4.7) (Fig. 5a).

35 zircon grains and 35 spots were analyzed for sample ZK4401-1 of fine-grained biotite monzogranite. 29 of the 35 grains yielded a $^{206}Pb/^{238}U$–$^{207}Pb/^{238}U$ concordia age of 58.66 ± 0.90 Ma (n = 29, MSWD = 0.76), and 29 spots yielded a weighted mean $^{206}Pb/^{238}U$ age of 57.02 ± 0.42 Ma (n = 29, MSWD = 1.03) (Fig. 5b).

Sample YT4440 of fine- and medium-grained biotite granodiorite had 35 zircon grains and 35 spots analyzed. 27 of them yielded a weighted mean $^{206}Pb/^{238}U$ age of 56.1 ± 1.1 Ma (n = 27, MSWD = 2.0) (Fig. 5c).

5.2. Molybdenite Re–Os geochronology

Table 2 shows the analytical results of Re–Os isotope for five molybdenite samples. Re content of the samples was relatively high and varied in a range of 998.49–34333.82 ng/g. Re^{187} content is between 625.05 and 21492.97 ng/g and Os^{187} between 0.65 and 22.24 ng/g. The five molybdenite samples yielded model ages of 62.3 ± 0.5 Ma, 62.6 ± 0.6 Ma, 62.7 ± 1.1 Ma, 62.7 ± 1.1 Ma and 62.8 ± 0.7 Ma. Their isochron age is 63.2 ± 3.2 Ma (MSWD = 3.8) and weighted mean age 62.9 ± 1.0 Ma (Fig. 6).

5.3. Geochemical compositions of ilvaite

Table 3 shows chemical composition of ilvaite from microprobe analysis. Their Al_2O_3 and SiO_2 content was similar, but their content of MnO and FeO demonstrates a large difference between the first- and second-generation phases. The second-generation ilvaite contains higher F (0.06–1.03 wt.%) and TiO_2 (0–0.10 wt.%) and lower Cl (0–0.03 wt.%) than the first-generation ilvaite (0–0.79 wt.% of F, 0–0.02 wt.% of TiO_2, and 0–0.13 wt.% of Cl). Content of Al_2O_3 and SiO_2 of the first-generation varied in a range of 0.07–0.25 wt.% and 28.48–31.34 wt.% respectively, while those of the second-generation in a range of 0.07–0.34 wt.% and 28.83–30.12 wt.%. In addition, the first-generation ilvaite showed MnO content of 1.707–5.30 wt.%, FeO content of 46.50–50.90 wt.%, while the second-generation contained 1.10–3.50 wt.% MnO and 48.69–51.42 wt.% FeO.

6. Discussion

6.1. Timing of magmatism and mineralization of the Hahaigang W–Mo deposit

Unlike normal skarn deposits that occur in contacts between felsic-intermediate plutons and their carbonate country rocks, the Hahaigang W–Mo polymetallic skarn deposit shows no close spatial relationship with carbonate rock. As shown in Fig. 3 and described in a previous section, the deposit is strictly controlled by the NE-striking Dalong fault zone. In addition, the obtained Re–Os isochron age 63.2 ± 3.2 Ma from

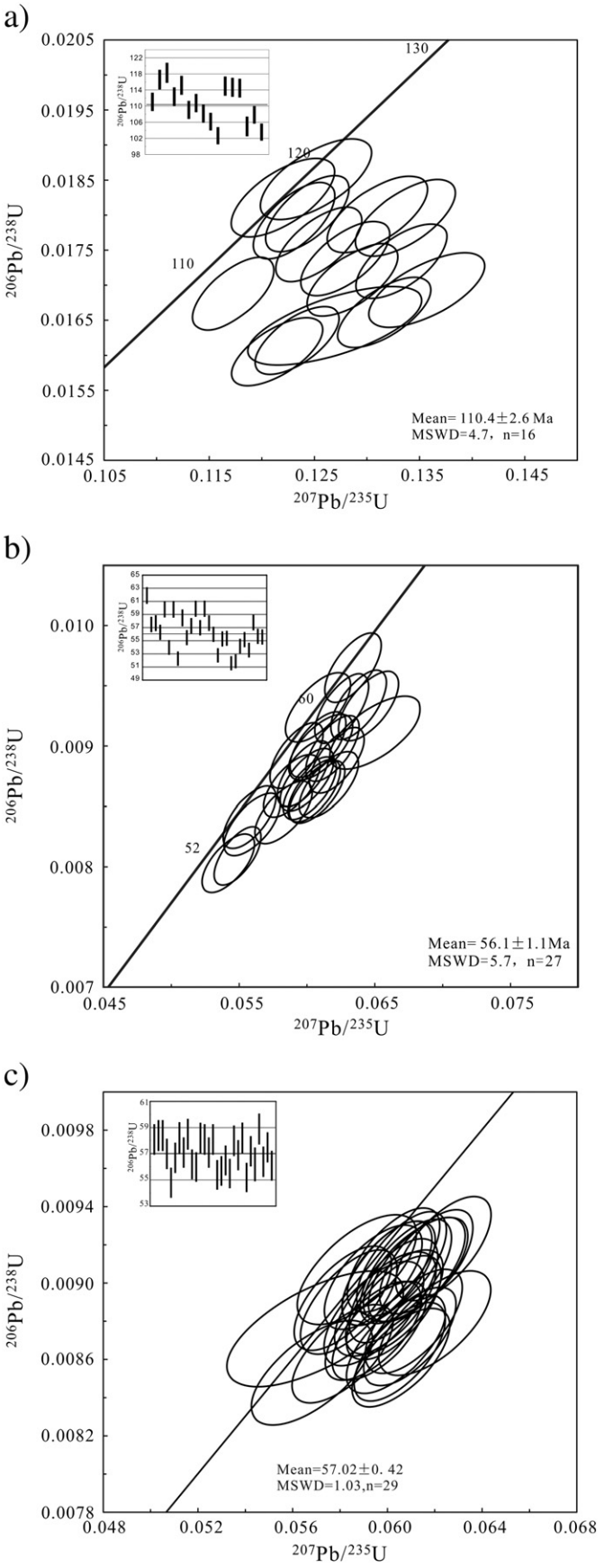

Fig. 5. Concordia plots of zircon U–Pb data for (a) mylonited granite porphyry (sample ZK5202-1), (b) biotite monzogranite (sample ZK4401-1), and (c) granodiorite (sample YT4440-1).

Table 2
Re–Os data of molybdenite from Hahaigang W–Mo deposit.

Samples	Os^{187} (ng/g)	Os (ng/g)	Re (ng/g)	^{187}Re (ng/g)	Model ages (Ma)
2301	22.24 ± 0.17	0.047 ± 0.074	34333.82 ± 638.48	21492.97 ± 399.69	62.3 ± 0.5
4200	9.02 ± 0.08	0.050 ± 0.007	13868.89 ± 219.89	8681.93 ± 137.65	62.6 ± 0.6
4200-2b	6.17 ± 0.10	0.356 ± 0.041	9467.16 ± 147.68	5926.44 ± 92.45	62.7 ± 1.1
4200-2c	14.49 ± 0.11	0.288 ± 0.038	21774.66 ± 138.66	13630.94 ± 86.80	64.0 ± 0.5
4520-2b	0.65 ± 0.01	0.304 ± 0.031	998.49 ± 14.55	625.05 ± 9.11	62.8 ± 0.7

the five molybdenite samples, which represents the mineralization age of the deposit, shows considerable discrepancy with the obtained U–Pb ages of the igneous plutons around the deposit. For example, the fine-grained biotite monzogranite has a $^{206}Pb/^{238}U$–$^{207}Pb/^{238}U$ concordia age of 58.66 ± 0.90 Ma and a weighted mean $^{206}Pb/^{238}U$ age of 57.02 ± 0.42 Ma, and the fine- and medium-grained biotite granodiorite has a weighted mean $^{206}Pb/^{238}U$ age of 56.1 ± 1.1 Ma; both are younger than the mineralization age. The $^{206}Pb/^{238}U$–$^{207}Pb/^{238}U$ concordia age of 109.1 ± 8.9 Ma and weighted mean $^{206}Pb/^{238}U$ age of 114.0 ± 2.6 Ma of the granite porphyry are much older than the mineralization age. It was emplaced long before the W–Mo mineralization and prior to the India–Eurasia collision; and tectonically it could be a product of the Andean-type Tethys oceanic subduction, which resulted in an Andean-type Gangdese magmatic arc in the Cretaceous time. The monzogranite and granodiorite plutons that were emplaced after the W–Mo mineralization could be products of the continued India–Eurasia collision active until the end of the Paleocene. According to Xu et al. (2012), both the pre-collision Andean-type subduction and the syn-collision magmatism produced a rather complex Gangdese magmatic arc, as confirmed by the geochronological data presented in this paper.

Since neither the exposed granitic plutons nor the plutons intersected by drilling (which provided drill core samples ZK4401-1 and ZK5202-1 were collected) in Hahaigang district was coeval with the Hahaigang W–Mo mineralization. Therefore, it is suggested that the W–Mo polymetallic mineralization could be related to a suspected, deep-seated syn-collision pluton that is not exposed in the Hahaigang district.

The pre-W–Mo mineralization granite porphyry experienced a ductile shearing event locally resulting in the formation of mylonites. Pyrite grains from the skarn ores also show ductile deformation, indicating that the regional ductile shear deformation took place either simultaneously with or after the W–Mo mineralization. This deformation event could have resulted from the regional orogenic process of the India–Eurasia collision that initiated around 65 Ma (Hou et al., 2006a, 2006b, 2006c, 2009; Mo et al., 2003; Wang et al., 2003). The molybdenite mineralization age of 63.2 ± 3.2 Ma obtained from this study suggests that the Hahaigang W–Mo polymetallic skarn deposit was generated during the early and/or main India–Eurasia collision. A recent molybdenite Re–Os dating of the Yaguila Pb–Zn–Mo deposit which is located in the same mineralization belt as the Hahaigang deposit (see Fig. 1) by Gao et al. (2011) yielded a molybdenite model age of 64.27 ± 0.90–65.97 ± 1.13 Ma and an isochron age of 65.0 ± 1.9 Ma. The ages of both Yaguila Pb–Zn–Mo deposit and Hahaigang W–Mo polymetallic deposit suggest a regional Mo-related mineralization event during the early and/or main India–Eurasia collision.

As indicated by Hou et al. (2006a, 2009), the mineralization related to the main collision was typically of a Cu–Au–Mo–Pb–Zn metal assemblage. This study, however, suggests that a W–Mo mineralization could have also resulted from the main India–Eurasia collision, even though it is unusual in the Gangese metallogenic belt.

6.2. F–Ca–Fe-rich hydrothermal fluids and the formation of the Hahaigang W–Mo deposit

Ca-rich skarn mineral assemblages such as Ca-bearing garnet, chlorite, and ilvaite (Meinert et al., 2005; Petersen et al., 1995; Ussing, 1912) that are related to late-stage magmatic and hydrothermal processes are generally observed in skarns produced by contact metasomatism between igneous intrusions and their carbonate country rocks (Einaudi and Burt, 1982; Einaudi et al, 1981; Meinert et al., 2005). The so-called “stratiform skarns” may result from submarine exhalation and other non-magmatic processes (Meinert, 1992; Meinert et al., 2005). According to Shimazaki (1982) and Graser and Markl (2008), skarns could be also produced by chemical reactions between Ca–Fe-rich hydrothermal fluids and Al-bearing sedimentary rocks. Examples include the Sasano Cu-bearing skarn of the Yoshioka deposit of Japan and the Ca-rich skarn of the Ilimaussaq complex of Southern Greenland (Graser and Markl, 2008; Shimazaki, 1982).

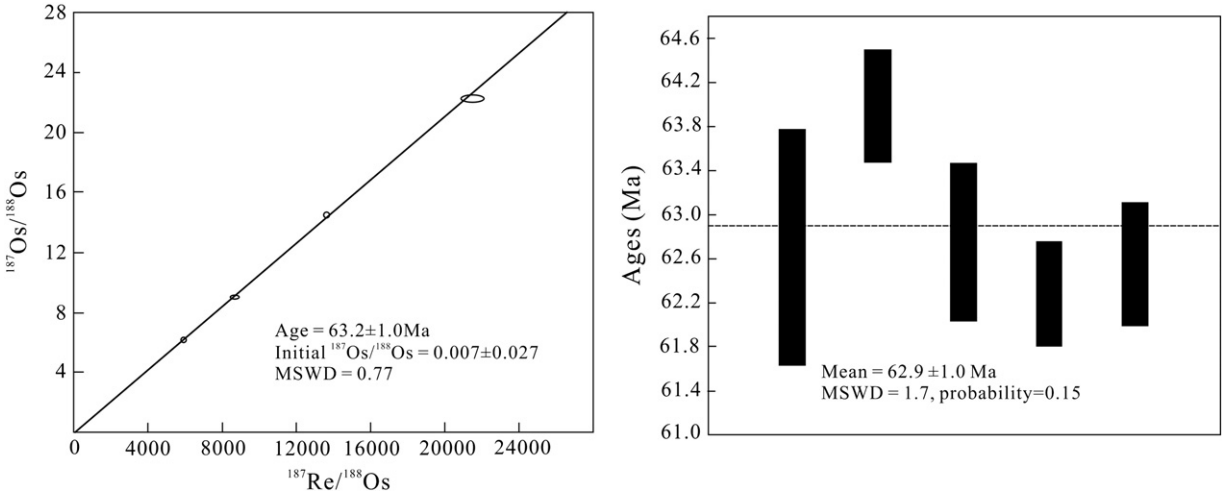

Fig. 6. Re–Os isochron age and weighted mean age of molybdenite.

Table 3
Representative microprobe data of ilvaite from the skarns in Hahaigang W–Mo deposit.

Samples	Generation	CaO	P_2O_5	La_2O_3	Ce_2O_3	Nd_2O_3	F	Cl	Na_2O	K_2O	MgO	Al_2O_3	SiO_2	TiO_2	Cr_2O_3	FeO	MnO	Total
5-1-11	Early	13.951	0.012	0	0	0.050	0.251	0.015	0	0.001	0.010	0.173	29.066	0.012	0.003	50.217	2.292	96.054
5-1-12	Early	14.170	0	0.068	0	0	0.61	0	0.018	0	0.010	0.152	28.478	0.013	0.006	49.287	1.707	94.520
5-2-3	Early	14.172	0.013	0.018	0.084	0	0.554	0.006	0.012	0	0.023	0.070	29.163	0	0	47.013	4.398	95.527
5-2-4	Early	13.524	0.008	0.042	0	0.011	0.464	0.014	0	0.005	0.038	0.204	29.372	0.005	0	46.496	5.297	95.480
5-2-5	Early	13.202	0.030	0.119	0.023	0.022	0.785	0.007	0.004	0.018	0.019	0.254	29.104	0.010	0.013	48.859	3.706	96.174
5-4-1	Early	14.382	0.020	0	0	0.074	0.557	0	0	0.003	0.012	0.079	29.594	0.004	0.008	50.014	2.015	96.762
5-4-3	Early	13.953	0.040	0	0	0.002	0.366	0	0.018	0	0	0.241	29.904	0	0.009	49.545	2.384	96.463
5-5-15	Early	12.634	0.030	0.089	0.016	0.126	0.027	0	0	0	0.028	0.218	30.508	0	0	48.901	5.234	97.904
5-5-16	Early	12.976	0	0.067	0	0	0	0.002	0	0	0	0.193	29.572	0.055	0	49.023	4.486	96.406
5-5-17	Early	13.135	0	0	0	0	0	0.115	0.015	0.021	0	0.252	31.337	0	0.336	48.623	3.541	97.460
5-5-24	Early	13.559	0	0	0.125	0	0	0	0.006	0	0.005	0.179	30.385	0.017	0.025	48.573	4.788	97.695
5-5-25	Early	13.922	0.015	0.156	0	0	0.062	0	0	0	0.025	0.185	30.993	0.001	0.003	50.893	1.973	98.257
5-1-2	Late	14.233	0	0.015	0	0.053	0.506	0.012	0.03	0	0.009	0.150	28.739	0.013	0	50.175	1.825	95.760
5-1-3	Late	14.506	0	0.016	0	0	0.056	0.016	0	0.008	0.010	0.220	29.463	0.002	0.006	49.935	1.82	96.059
5-1-4	Late	14.175	0	0.046	0	0	0.773	0.014	0	0.005	0.004	0.071	29.392	0.009	0	48.690	3.502	96.682
5-5-1	Late	13.897	0.009	0	0	0	0.807	0.032	0	0.008	0	0.288	29.253	0.011	0	49.610	1.860	95.776
5-5-2	Late	13.712	0.008	0	0.116	0	0.962	0.007	0.082	0.014	0.016	0.189	28.83	0.003	0.035	50.623	1.446	96.043
5-5-3	Late	14.017	0.006	0	0	0.003	0.425	0.002	0.038	0.009	0.027	0.322	29.278	0.005	0.034	49.640	2.327	96.133
8-1-1	Late	14.737	0.047	0.148	0	0	1.033	0.001	0	0	0	0.184	29.68	0.102	0	49.973	1.870	97.775
8-1-2	Late	13.736	0	0	0.130	0	0.897	0	0	0	0	0.340	29.617	0.023	0.018	50.955	1.279	96.996
8-2-2	Late	14.434	0	0	0.028	0	0.967	0.005	0	0	0	0.114	28.839	0	0.028	50.759	1.622	96.797
8-2-4	Late	14.480	0	0	0.093	0.008	0.790	0	0.019	0.002	0	0.253	29.754	0.016	0.003	51.038	1.097	97.551
8-2-5	Late	14.700	0.024	0	0	0	0.568	0.005	0	0	0.006	0.267	30.115	0.004	0.009	51.330	1.128	98.155
8-2-6	Late	14.164	0.002	0	0	0.064	0.414	0.014	0	0	0	0.160	29.329	0.021	0.010	51.423	1.291	96.890

Ilvaite is a Ca- and Fe-rich skarn mineral and is not commonly seen in skarns compared to other common skarn minerals such as garnet, diopside, and actinolite. However, according to Franchini et al. (2002), Einaudi et al. (1981), and Meinert et al. (2005), ilvaite could be found in Zn–Pb, Fe, and Au ores, as well as Sn–W–F(Be) skarns. Chemical composition and variation of less-abundant skarn minerals, e.g., ilvaite, might provide important constraints on skarn genesis and mineralization environment. For example, Franchini et al. (2002) reported ilvaite in skarn-type gold ores, analyzed its geochemical composition, and compared it with ilvaite found in skarn-type Zn, Fe, and Sn ores (Fig. 7). It is suggested that geochemical features of ilvaite could be used to help identify deposit types of skarn ores and provide useful information on ore-forming geologic and geochemical environment.

Detailed mapping at the Hahaigang deposit has delineated several types of skarns. They include garnet–diopside skarn, diopside–garnet skarn, chloritized garnet skarn, diopside skarn, magnetite–garnet skarn, and pyrrhotite–garnet skarn. They show a medium to coarse-grained granoblastic texture and a massive or banded structure. In addition to common skarn minerals garnet and diopside, the skarns also contain ilvaite and fluorite at the deposit.

The country rock of the Hahaigang deposit is dominantly the Lower-Permian Pangna Group clastic sedimentary rocks without any carbonate component. The Hahaigang skarn is therefore not carbonate-related skarn, and the ilvaite found within the Hahaigang skarns is obviously not produced by contact metasomatism between carbonates and an igneous pluton. Detailed mapping and observation in the deposit clearly reveal that the skarn ore bodies are controlled within the NE-striking Dalong fault zone, and the faulted Lower-Permian Pangna Group quartz sandstone within the fault zone serves as host rock. The Hahaigang skarn is not “stratified skarn” either, probably because it is controlled by the fault zone instead of sedimentary bedding, and no exhalative chemical sediments have been ever found in the deposit. We argue that the ilvaite and other skarn minerals diopside and garnet are likely product of chemical reactions between hydrothermal fluids and the quartz-feldspathic country rocks, as seen in Ca-rich skarns of the Ilmaussag complex of southern Greenland (Graser and Markl, 2008). The formation of the skarn minerals and fluorite that are present as veins suggests that the hydrothermal fluids were Ca–F–Fe-rich fluids. As shown in Table 3, the Hahaigang ilvaite is characterized by relatively high content of F, which is typical of the Hahaigang W–Mo ores. However, ilvaite reported from skarns elsewhere contains little or no F. As shown in Fig. 7 and Table 3, the second-generation ilvaite in Hahaigang deposit contains relatively higher amounts of F, Fe, and Ca but lesser amounts of Mn than the earlier, first-generation ilvaite, reflecting a systematic change of abundance of the elements in the hydrothermal fluids that could be derived from unexposed magma sources. It indicates that the fluids associated with the second-generation ilvaite became more Ca–Fe–F-rich.

6.3. Tectonic and geological setting of the Hahaigang W–Mo mineralization

The Tibetan orogen has undergone periodic tectono-magmatic evolution, including a main-collisional convergent setting (~65–41 Ma), a late-collisional transform structural setting (~40–26 Ma), and a post-collisional crustal extension setting (~25–0 Ma) (Hou et al., 2006a, 2006b). A corresponding tectonic stress regime has changed from an intense impact (~65 to 54 Ma), relaxation (~53 to 41 Ma), and transpression (~40 to 30 Ma) to transtension (~30 to 26 Ma), and a change from N–S compression (N18 Ma) to E–W extension (S18 Ma) (Fig. 2; Hou et al., 2006a, 2013). Each period was associated with distinct metallogenic processes that produced specific mineralized systems (Fig. 2) (Hou et al., 2006a, 2009). The India–Eurasia collision initiated at about 65 Ma, followed by significant high-angle slab penetration, slab detachment, underplating, and large-volume magmatism; subsequent granitic plutonism and associated hydrothermal activity produced orogen-scale polymetallic mineralization along the length of the collision zone (Hou et al., 2009; Mo et al., 2003; Wang et al., 2003). Based on Hou et al. (2006a), the main collision resulted in four mineralization events: 1) Sn-REE mineralization associated with granitoids derived from continental crust; 2) Cu–Au–Mo mineralization associated with granitoids produced by a mixing of magmas derived from continental crust and mantle sources; 3) Au mineralization related to orogenic ductile shear zones; and 4) Cu–Au mineralization related to crust shortening and uplifting (Fig. 2).

The Hahaigang molybdenite Re–Os age of 63.2 ± 3.2 Ma reported in this study demonstrates that the formation of the Hahaigang W–Mo polymetallic deposit must be related to the main collision. It is therefore suggested that a W mineralization event took place during the main India–Eurasia collision. This is further confirmed by a recent report of molybdenite Re–Os ages of Yaguila Pb–Zn–Mo deposit which is also

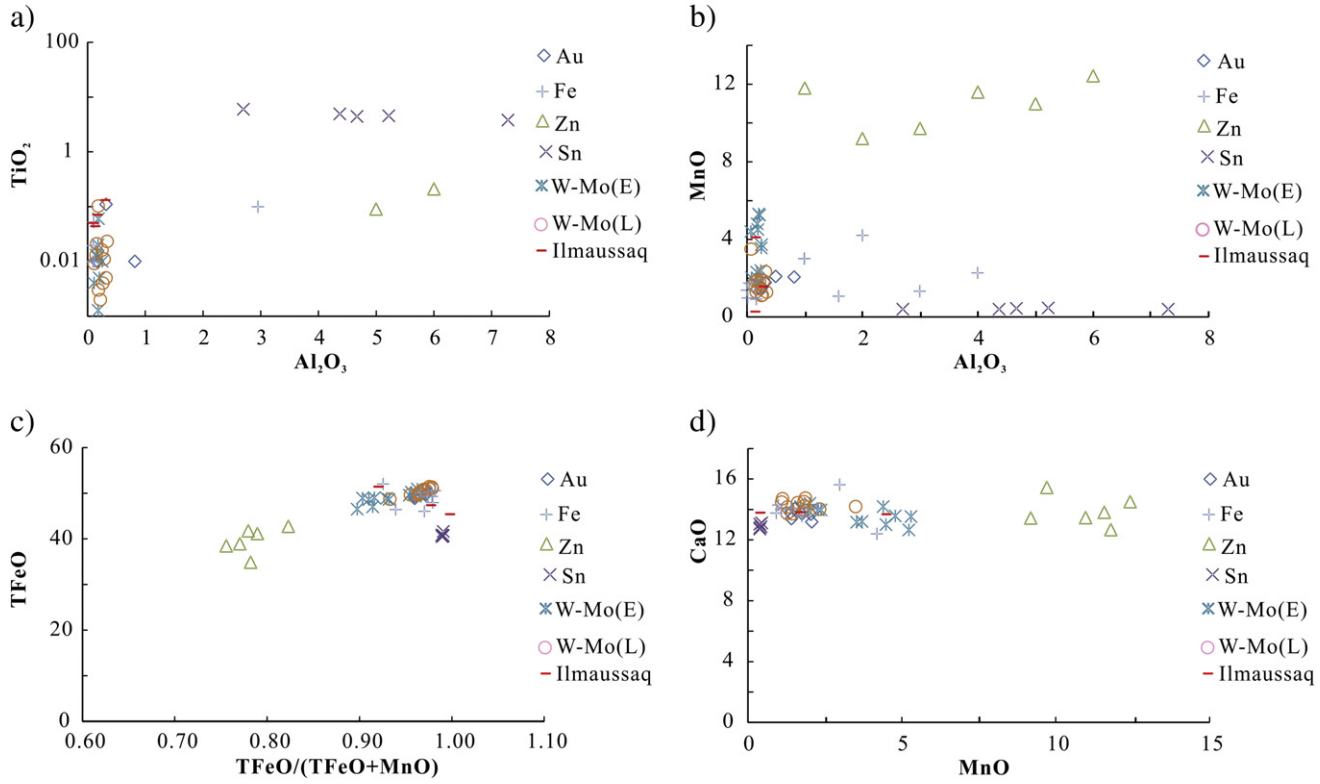

Fig. 7. (a) FeO vs. FeO / (FeO + MnO) (unit: wt.%) diagram illustrating Fe and Mn variations of ilvaite as a function of skarn types from different ores. (b) MnO vs. Al_2O_3 (unit: wt.%) diagram illustrating Mn and Al variations of ilvaite as a function of skarn types from different ores. (c) MnO vs. CaO (unit: wt.%) diagram illustrating MnO and Ca variations of ilvaite as a function of skarn types from different ores. (d) TiO_2 vs. Al_2O_3 (unit: wt.%) diagram illustrating Ti and Al variations of ilvaite as a function of skarn types from different ores. See text for explanation. Data sources: gold (Au) skarn (Franchini et al., 2002); Fe skarn (Gole, 1981; Meinert, 1984; Tang, 2010; Tang et al., 2011); Zn skarn (Ashley, 1980; Meinert, 1987); Sn skarn (Kwak, 1983); Ilimaussaq complex (Graser and Markl, 2008); W–Mo skarn, from this study, W–Mo(E) for early, first-generation ilvaite; W–Mo(L) for late, second-generation ilvaite (modified after Franchini et al., 2002).

located in the same mineralization belt as the Hahaigang deposit (see Fig. 1), i.e., a molybdenite model age of 64.27 ± 0.90–65.97 ± 1.13 Ma and an isochron age of 65.0 ± 1.9 Ma (Gao et al., 2011).

With continuing collision and accompanied tectono-magmatic activities, large-scale ductile shearing took place within the Lhasa terrane and the Gangdese tectono-magmatic belt, particularly along the southern margin of the Gangdese belt. The ductile shearing produced ENE-striking sinistral ductile shear zones that steeply dip toward north. A number of ENE-striking and NW-striking brittle fault zones were also developed (Hou et al., 2006a, 2006b, 2006c). The ductile shearing and faulting were accompanied by emplacement of large-volume muscovite granite plutons and slightly fewer monzogranite intrusions (Deng et al., 1996). Strike-slip faulting as a result of orthogonal compression during the main collision played a major role in controlling metallogenic processes (Yan and Huang, 2010). The Hahaigang deposit is located in an area where a number of EW-striking transpressional faults intersect with a number of SN-striking transtensional faults. The development of ductile shear zones and ENE-striking and NW-striking brittle faults resulted from orthogonal compression during the main collision, for example, the NE-striking Dalong fault in Hahaigang district provided a favorable structural environment for mineralization. The F–Fe–Ca-rich hydrothermal fluids which were most likely derived from deep-seated magmas, and ascended through the faults. Because neither of the two key ingredients for skarn mineral formation (i.e., existence of carbonate as country rock and an igneous intrusion) is present in the Hahaigang deposit, the Ca–Fe–F-rich hydrothermal fluids were a key factor for the formation of the skarn minerals at the deposit studied here. Reaction and metasomatism between the F–Fe–Ca-rich fluids and faulted quartzo-feldsparthic rocks of the Lower-Permian Pangna Group, e.g., quartz sandstone, produced the Hahaigang skarns and W–Mo mineralization.

7. Conclusions

(1) The ages of the igneous plutons exposed and encountered by drilling in the Hahaigang district are determined by zircon U–Pb LA–ICP–MS method in this study. The biotite monzogranite yields a $^{206}Pb/^{238}U$–$^{207}Pb/^{238}U$ concordia age of 58.66 ± 0.90 Ma and a weighted mean $^{206}Pb/^{238}U$ age of 57.02 ± 0.42 Ma. The granite porphyry yielded a $^{206}Pb/^{238}U$–$^{207}Pb/^{238}U$ concordia age of 109.1 ± 8.9 Ma and a weighted mean $^{206}Pb/^{238}U$ age of 114.0 ± 2.6 Ma. The biotite granodiorite yielded a weighted mean $^{206}Pb/^{238}U$ age of 56.1 ± 1.1 Ma. These ages indicate that the dated plutons in the deposit were emplaced either pre- or post-main India–Eurasia collision.

(2) A molybdenite isochron age of 63.2 ± 3.2 Ma from five molybdenite samples collected from the Hahaigang W–Mo polymetallic deposit was also obtained from this study by using Re–Os method. This W–Mo mineralization age is not coeval with any of the dated igneous plutons in the deposit. However, it demonstrates that the formation of the W–Mo mineralization occurred during the main India–Eurasia collision that was initiated around 65 Ma (Hou et al., 2006a, 2006b, 2006c; Mo et al., 2003; Wang et al., 2003) and lasted till 50–41 Ma (Decelles et al., 2004; Rowley, 1996). Although formation of the majority of polymetallic deposits within the Gangdese belt has been reported to be either pre- or post-main collision, it is evident from this study that the main collision also produced W–Mo mineralization, such as the Hahaigang W–Mo polymetallic deposit and the Yaguila Pb–Zn–Mo deposit.

(3) Ore bodies of the Hahaigang deposit are strictly confined within the NE-striking Dalong fault zone and are present as unusual skarn-type ores because no carbonates have been found in the deposit and vicinity. In addition to common skarn minerals such as

diopside and garnet observed in the deposit, ilvaite is also found as a skarn mineral in the deposit. Based on textural and microprobe geochemical analysis of the ilvaite that occurs as two generations in the skarn deposit, it is suggested that both generations of the ilvaite were related to Ca–Fe–F-rich hydrothermal fluids which could be derived from deep-seated magmas. The proposed scenario is that the ascent of the fluids was strictly controlled by the NE-striking Dalong fault zone, and chemical interaction and metasomatism between the fluids and the faulted quartzofeldspathic host rocks of the Lower-Permian Pangna Group within the fault zone produced the ilvaite-bearing skarns. The W–Mo polymetallic mineralization occurred concurrently with the skarnization and produced unusual skarn-type ores in the fault zone. The skarnization and mineralization occurred during the main India–Eurasia collision.

Acknowledgments

This study was financially supported by National Fundamental Research and Development Program of China (grant No. 2011CB403106), IGCP project (No. IGCP/SIDA-600), One Hundred Person Project of the Chinese Academy of Sciences, and National Natural Science Foundation of China (grant No. 41272112). We are grateful to Richard Goldfarb for his constructive help in improving the original manuscript. We thank Feng Zuohai for his assistance in fieldwork. Special thanks to Franco Pirajno, Brian Rusk and an anonymous reviewer for their constructive comments and suggestions, and also to David Putnam for helping with editing.

References

Ashley, P.M., 1980. Geology of the Ban Ban zinc deposit, a sulfide-bearing skarn, Southeast Queensland, Australia. Econ. Geol. 75, 15–29.
Blisniuk, P.M., Hacker, B.R., Glodny, J., Ratschbacher, L., Bi, S., Wu, Z., Mc Williams, M.O., Calvert, A., 2000. Crustal thinning in central Tibet since at least 13.5 Myr. Nature 412, 628–632.
Chu, M.F., Chung, S.L., Song, B., Liu, D.Y., O'Reilly, S.Y., Pearson, N.J., 2006. Zircon U–Pb and Hf isotope constraints on the Mesozoic tectonic and crustal evolution of southern Tibet. Geology 34, 745–748.
Chung, S.L., Chu, M.F., Zhang, Y.Q., Xie, Y.Q., Lo, C.H., Lee, T.Y., Lan, C.Y., Li, X.H., Zhang, Q., Wang, Y.Z., 2005. Tibetan tectonic evolution inferred from spatial and temporal variations in post-collisional magmatism. Earth Sci. Rev. 68, 173–196.
DeCelles, P.G., Gehrels, G.E., Najman, Y., Martin, A.J., Carter, A., Garzanti, E., 2004. Detrital geochronology and geochemistry of Cretaceous-Early Miocene strata of Nepal: implication for timing and diachroneity of initial Himalaya orogenesis. Earth Planet. Sci. Lett. 227, 313–330.
Deng, J.F., Zhou, H.L., Mo, X.X., 1996. Continental Root-Plume Tectonic of China: Key to the Continental Dynamics. Geological Publishing House, Beijing (345 pp.).
Ding, L., Kapp, P., Zhong, D.L., Deng, W.M., 2003. Cenozoic volcanism in Tibet: evidence for a transition from oceanic to continental subduction. J. Petrol. 44, 1833–1865.
Du, A.D., He, H.L., Yin, N.W., 1994. A study on the rhenium–osmium geochronometry of molybdenite. Acta Geol. Sin. 68 (4), 339–347.
Du, A.D., Zhao, D.M., Wang, S.X., Sun, D.Z., Liu, D.Y., 2001. Precise Re–Os dating for molybdenite by ID-NTIMS with Carius tube sample preparation. Rock Miner. Anal. 20 (4), 247–252.
Durr, S.B., 1996. Provenance of Xigaze fore-arc basin clastic rocks (Cretaceous, south Tibet). Geol. Soc. Am. Bull. 108, 669–684.
Einaudi, M.T., Burt, D.M., 1982. Introduction — terminology, classification, and composition of skarn deposits. Econ. Geol. 77, 745–754.
Einaudi, M.T., Meinert, L.D., Newberry, R.T., 1981. Skarn deposits. Econ. Geol. 317–391 (75th Anniversary Volume).
Franchini, M.B., Meinert, L.D., Valles, J.M., 2002. First occurrence of ilvaite in a gold skarn deposit. Econ. Geol. 97, 1119–1126.
Gao, Y.F., Wei, R.H., Hou, Z.Q., Tian, S.H., Zhao, R.S., 2008. Eocene high-MgO volcanism in southern Tibet: new constraints for mantle source characteristics and deep process. Lithos 105, 63–72.
Gao, Y.F., Yang, Z.S., Santosh, M., Hou, Z.Q., Wei, R.H., Tian, S.H., 2010. Adakitic rocks from slab melt-modified mantle sources in the continental collision zone of southern Tibet. Lithos 119, 651–663.
Gao, Y.M., Chen, Y.C., Tang, J.X., Li, C., Li, X.F., Gao, M., Cai, Z.C., 2011. Re–Os dating of molybdenite from the Yaguila Pb–Zn–Mo deposit in Gongbojiangda area, Tibet, and its geological significance. Geol. Bull. China 30 (7), 1027–1036.
Gole, M.J., 1981. Ca–Fe–Si skarn containing babingtonite: first known occurrence in Australia. Can. Mineral. 19, 26–277.
Graser, G., Markl, G., 2008. Ca-rich ilvaite–epidote–hydrogarnet endoskarns: a record of late magmatic fluid influx into the persodic Ilimaussaq complex, South Greenland. J. Petrol. 49, 239–265.
Guilin Research Institute of Geology for Mineral Resources, 2009. The Exploration Report on Hahaigang W–Mo Deposit in Tibet (Internal Publication).
Guynn, J.H., Kapp, P., Pullen, A., Heizler, M., Gehrels, G., Ding, L., 2006. Tibetan basement rocks near Amdo reveal "missing" Mesozoic tectonism along the Bangong suture, central Tibet. Geology 34, 505–508.
Hou, Z.Q., Gao, Y.F., Qu, X.M., Rui, Z.Y., Mo, X.X., 2004. Origin of adakitic intrusives generated during mid-Miocene east–west extension in southern Tibet. Earth Planet. Sci. Lett. 220, 139–155.
Hou, Z.Q., Mo, X.X., Yang, Z.M., Wang, A.J., Pang, G.T., Qu, X.M., Nie, F.J., 2006a. Metallogenesis in the Tibetan collision orogenic belt: tectonic setting, metallogenic epoch and deposit type. Geol. China 33, 348–359.
Hou, Z.Q., Yang, Z.S., Xu, W.Y., Mo, X.X., Deng, L., Gao, Y.F., 2006b. Metallogenesis in Tibetan collisional orogenic belt: mineralization in main collisional orogenic setting. Miner. Depos. 25 (4), 337–358.
Hou, Z.Q., Zhao, Z.D., Gao, Y.F., Yang, Z.M., Jiang, W., 2006c. Tearing and subduction of the Indian continental slab: evidence from Cenozoic Gangdese igneous rocks in Tibet. Acta Petrol. Sin. 22, 761–774 (in Chinese with English abstract).
Hou, Z.Q., Yang, Z.M., Qu, X.M., Meng, X.J., Li, Z.Q., Beaudoin, G., Rui, Z.Y., Gao, Y.F., 2009. The Miocene Gangdese porphyry copper belt generated during post-collisional extension in the Tibetan Orogen. Ore Geol. Rev. 36, 25–51.
Hou, Z.Q., Zheng, Y.C., Yang, Z.M., Rui, Z.Y., Zhao, Z.D., Jiang, S.Y., Qu, X.M., Sun, Q.Z., 2013. Contribution of mantle components within juvenile lower-crust to collisional zone porphyry Cu systems in Tibet. Mineral. Deposita 48, 173–192.
Jian, P., Liu, D.Y., Sun, X.M., 2003. SHRIMP dating of Carboniferous Jinshajiang ophiolite in western Yunnan and Sichuan: geochronological constraints on the evolution of the paleo-Tethys oceanic crust. Acta Geol. Sin. 77, 217–277 (in Chinese with English abstract).
Kwak, T.P., 1983. The geology and geochemistry of the zoned, Sn–W–F–Be skarns at Mt. Lindsay, Tasmania, Australia. Econ. Geol. 78, 1440–1465.
Lee, T.Y., Lawver, L.A., 1995. Cenozoic plate reconstruction of the South China Sea region. Tectonophysics 251, 85–138.
Meinert, L.D., 1984. Mineralogy and petrology of iron skarns in western British Columbia, Canada. Econ. Geol. 79, 869–882.
Meinert, L.D., 1987. Skarn zonation and fluid evolution in the Groundhog mine, Central Mining district, New Mexico. Econ. Geol. 82, 523–545.
Meinert, L.D., 1992. Skarn and Skarn deposit. Geosci. Can. 19, 145–162.
Meinert, L.D., Dipple, G.M., Nicolescu, S., 2005. World skarn deposits. Econ. Geol. 299–336 (100th anniversary volume).
Miller, C., Schuster, R., Klotzli, U., Frank, W., Purtscher, F., 1999. Postcollisional potassic and ultrapotassic magmatism in SW Tibet: geochemical and Sr–Nd–Pb–O isotopic constraints for mantle source characteristics and petrogenesis. J. Petrol. 40, 1399–1424.
Mo, X.X., Zhao, Z.D., Deng, J.F., Dong, G.C., Zhou, S., Guo, T.Y., Zhang, S.Q., Wang, L.L., 2003. Response of volcanism to the India–Asian collision. Earth Sci. Front. 10, 135–148 (in Chinese with English abstract).
Mo, X.X., Dong, Z., Zhou, Z., Zhou, S., Wang, L., Qiu, R., Zhang, F., 2005. Response of volcanism to the India–Asian collision. Earth Sci. Front. 10, 135–148 (in Chinese with English abstract).
Mo, X.X., Hou, Z.Q., Niu, Y.L., Dong, G.C., Qu, X.M., Zhao, Z.D., Yang, Z.M., 2007. Mantle contributions to crustal thickening in south Tibet in response to the India–Asia collision. Lithos 96, 225–242.
Mo, X.X., Niu, Y.L., Dong, G.C., Dong, G.C., Zhao, Z.D., Hou, Z.Q., Ke, S., 2008. Contribution of syncollisional felsic magmatism to continental crust growth: a case study of the Paleogene Linzizong volcanic succession in southern Tibet. Chem. Geol. 250, 49–67.
Pan, G.T., Mo, X.X., Hou, Z.Q., Zhu, D.C., Wang, L.Q., Li, G.M., Zhao, Z.D., Geng, Q.R., Liao, Z.L., 2006. Spatial–temporal framework of the Gangdese Orogenic Belt and its evolution. Acta Petrol. Sin. 22 (3), 521–531 (in Chinese with English abstract).
Petersen, O.V., Micheelsen, H.I., Leonardsen, E.S., 1995. Bavenite, $Ca_4Be_3Al[Si_9O_{25}(OH)_3]$, from the Ilimaussaq alkaline complex, South Greenland. Neues Jb. Mineral. Monat. 7, 321–335.
Rowley, D.B., 1996. Age of initiation of collision between India and Asia: A review of stratigraphic data. Earth Planet. Sci. Lett. 145, 1–13.
Qu, X.M., Hou, Z.Q., Zaw, K., Mo, X.X., Xu, W.Y., Xin, H.B., 2009. A large-scale copper ore-forming event accompanying rapid uplift of the southern Tibetan Plateau: evidence from zircon SHRIMP U–Pb dating and LA ICP–MS analysis. Ore Geol. Rev. 36, 52–64.
Shimazaki, H., 1982. The Sasano hastingsite-bearing copper skarn deposit formed in aluminous sediment, at the Yoshioka mine, Japan. Econ. Geol. 77, 868–876.
Tang, P.Z., 2010. The Geochemistry Characteristics of Cihai Iron Deposit in Xinjiang. (Master dissertation) Kunming University of Science and Technology, Kunming.
Tang, P.Z., Wang, Y.W., Wang, J.P., Long, L.Y., Zhang, H.Q., Liao, Z., 2011. The discovery of ilvaite and its geological significance. Acta Mineral. Sin. 31 (1), 9–16.
Turner, S., Hawkesworth, G., Liu, J., Rogers, N., Kelley, S., Calsteren, P.V., 1993. Timing of Tibetan uplift constrained by analysis of volcanic rocks. Nature 364, 50–54.
Ussing, N.V., 1912. Geology of the country around Julianehaab, Greenland. Medd. Gronland 38 (426 pp.).
Wang, C.S., Li, X.H., Hu, X.M., 2003. Age of initial collision of India with Asia: review and constraints from sedimentary in Southern Tibet. Acta Geol. Sin. 77, 16–24.
Wang, Q., Wyman, D.A., Xu, J.F., Dong, Y.H., Vasconcelos, P.M., Pearson, N., Wan, Y.S., Dong, H., Li, C.F., Yu, Y.S., Zhu, T.X., Feng, X.T., Zhang, Q.Y., Zi, F., Chu, Z.Y., 2008. Eocene melting of subducting continental crust and early uplifting of central Tibet: evidence from central-western Qiangtang high-K calc-alkaline andesites, dacites and rhyolites. Earth Planet. Sci. Lett. 272, 158–171.
Williams, H.M., Turner, S.P., Pearce, J.A., Kelley, S.P., Harris, N.B.W., 2004. Nature of the source regions for post-collisional, potassic magmatism in Southern and Northern Tibet from geochemical variations and inverse trace element modeling. J. Petrol. 45, 555–607.

Xu, W.C., Zhang, H.F., Guo, L., Yuan, H.L., 2010. Miocene high Sr/Y magmatism, south Tibet: product of partial melting of subducted Indian continental crust and its tectonic implication. Lithos 114, 293–306.
Xu, Z.Q., Yang, J.S., Li, W.C., Zeng, L.S., Xu, C.P., 2012. Tectonic background of important metallogeic belts in the southern and southeastern Tibetan Plateau and ore prospecting. Acta Geol. Sin. 86 (12), 1857–1868.
Yan, X.Y., Huang, X.F., 2010. Discovery of large Zedang tungsten–copper–molybdenum orefields, Eastern Gangdese Arc, and new understanding on strike-slip type epicontinental mineralization. Geol. Rev. 56 (1), 9–20.
Yan, X.Y., Huang, X.F., Du, A.D., 2010. Re–Os ages of large tungsten, copper and molybdenum deposit in the Zetang orefield, Gangdese and marginal strike-slip transforming metallogenesis. Acta Geol. Sin. 84 (3), 398–405.
Yin, A., Harrison, T.M., 2000. Geologic evolution of the Himalayan–Tibetan orogen. Annu. Rev. Earth Planet. Sci. 28, 211–280.
Zhao, Z.D., Mo, X.X., Dilek, Y., Niu, Y.L., DePaolo, D.J., Robinson, P., Zhu, D.C., Sun, C.G., Dong, G.C., Zhou, S., Luo, Z.H., Hou, Z.Q., 2009. Geochemical and Sr–Nd–Pb–O isotopic compositions of the postcollisional ultrapotassic magmatism in SW Tibet: petrogenesis and implications for India intra-continental subduction beneath southern Tibet. Lithos 113, 190–212.